Interfacial hydroelastic hydraulic falls and trapped waves over bottom obstacles

Jin Chai,[1,2] Zhan Wang,[1,2,a)] and Emilian Părău[3]
[1)]*Institute of Mechanics, Chinese Academy of Sciences, Beijing 100190, PR China*
[2)]*School of Engineering Science, University of Chinese Academy of Sciences, Beijing 100049, PR China*
[3)]*School of Mathematics, University of East Anglia, Norwich NR4 7TJ, UK*

(Dated: October 10, 2022)

Steady nonlinear flexural-gravity hydraulic falls on the interface of a two-layer density stratified flow past a submerged obstruction on the bottom of a channel are considered. The fluid is assumed to be ideal, and the flow is irrotational. We extend the previous works[13,46] by including the effect of hydroelasticity. The interface is modeled as a thin elastic shell with the Cosserat theory. The boundary integral equation techniques are employed to find steady solutions by numerically solving the full Euler equations. New solutions characterized by subcritical flow upstream with different depth ratios (thick upper layer, thick bottom layer, or critical depth) are found, and the effects of the aspect ratio of obstruction are investigated. By introducing a second obstruction downstream, solutions characterized by a train of trapped waves are sought with wavelength coherent with the prediction of the linear dispersion relation. In addition, solutions with a soliton-like form and oscillatory decaying tails are found when the sheet rigidity is small and the second obstruction is placed upstream.

I. INTRODUCTION

The problems of hydroelasticity, which bring together hydrodynamics and elastic theories, are essential in many industrial applications such as biology, medicine, polar engineering, and the like[28,42]. The dynamics of a system of hydroelasticity are coupled, which means the deformations of the elastic body respond to hydrodynamic excitations, and simultaneously, the excitations are modified by the deformations. Theories and numerical methods for these problems with coupled fluid motion and elastic deformations are still under development and draw growing attention.

Most existing works focus on a single-layer system covered by an elastic plate or membrane. The elasticity models evolved, and different types of steady wave solutions were investigated, representing the hydroelastic waves in the presence of thin ice sheets in cold polar regions or large floating structures[35,42,43]. For small deformations, the linear theory of elastic plate has been widely used. However, it fails when the moving load is near the critical speed where the group velocity is equal to the phase velocity, and the nonlinear effects should be considered. Moreover, considering the impact of global warming, the linear theory became more limited[42], and the Kirchhoff-Love plate theory, the simplest nonlinear elastic model, was developed. Traveling-wave solutions, including periodic waves, solitary waves with oscillatory decaying tails, and generalized solitary waves, were numerically found in this model[18,19,32,38,45]. Due to the lack of energy conservation in the Kirchhoff-Love model, Toland[44] used the special Cosserat theory of hyperelastic shells to model the coupling between the elastic body and the fluid motion, which features a clear Hamiltonian structure. Guyenne and Părău[24] derived the cubic nonlinear Schrödinger (NLS) equation for small-amplitude wavepackets in deep water based on the Toland model. Elevation and depression wavepacket solitary waves were obtained by computing the fully nonlinear equations. Wang *et al.*[48] complemented the results in Ref. 24 with new elevation solitary waves by using an efficient computation method to trace the bifurcation path. Guyenne and Părău[36] considered the same problem in finite depth. They derived two weakly nonlinear models: a fifth-order Korteweg-de Vries (KdV) equation and a cubic NLS equation for long and short waves, respectively, and comparisons between fully nonlinear results and weakly nonlinear solutions were discussed. Xia and Shen[49] also derived the fifth-order KdV equation under the shallow-water approximation. Gao *et al.*[21] computed a new family of asymmetric solitary waves and investigated their stability subject to longitudinal perturbations. In addition to solitary waves, Page and Părău[35] found steady flexural-gravity hydraulic falls past an obstruction on bottom topography by a boundary integral equation method and investigated trapped waves between two successive obstacles. They also compared their numerical results with previous experiments.

Other physical problems and applications in which an elastic plate separates two fluids are also worth attention. Several analogous examples include flat-type fuel assemblies used in the cooling systems of nuclear reactors[27] and flapping flags or flaps in a channel flow[2,25,26]. An elastic plate under water can also be applied to wave energy devices as a wave carpet. Hot topics have recently focused on using submerged flexible plates or membranes instead of floating or vertical ones as breakwaters or wave barriers. That is because they can be designed with a higher wave-blocking efficiency and do not hamper the passage of ships and currents[8,33]. In this situation where the elastic plate plays a role as a wave barrier or attenuator, the influence exerted by an obstruction on bottom topography can be important and might need to be considered. Furthermore, it is also mentioned by Părău[39] that on the icy moons of Jupiter and Saturn, oceans with layered structures separated by ice shells are hypothesized to exist. Therefore, there has been a growing interest in interfacial hy-

[a)]Corresponding author: zwang@imech.ac.cn

draulic waves in a two-layer fluid system. The well-posedness of two-dimensional hydroelastic waves in a thin elastic sheet (with or without mass) placed in potential flow has already been proved[3,30]. Akers *et al.*[1] used a global bifurcation theorem to find the periodic travelling interfacial hydroelastic waves under the assumption of infinite depth. Other works consider cases where the free surface and interface exist at the same time. Wang *et al.*[47] computed interfacial bright solitary waves and generalized solitary waves under a flexible elastic sheet, which models the stratified structure under an ice-covered ocean. Nonlinear travelling waves on a sheet of fluid between thin infinite elastic plates and the corresponding temporal evolution have been studied[6,12]. Părău[39] computed interfacial hydroelastic solitary waves in different configurations: the upper layer of infinite extent, the upper layer bounded by a rigid wall, or a second elastic plate. Comparisons among these configurations have been investigated and discussed.

The present work is concerned with a two-layer fluid system separated by an interface over the bottom topography. Hydraulic fall solutions of interfacial waves, which represent flow passing gradually from one depth to another and from subcritical to supercritical (or in reverse), are mainly considered. These solutions can also be regarded as critical states where they jump on a solitary wave solution and have a form of half solitary wave. Following the previous results on steady interfacial gravity waves[4,5,13,14,16,17,22,29,40,41,46], we have extended the configuration by including hydroelasticity on the interface using the nonlinear Toland beam theory. Boundary integral equation techniques are implemented, and different regimes divided by the depth ratio with subcritical flow upstream in the lower layer are considered. The formulation of the problem, including linear analysis and the numerical scheme, is presented in §2. Steady hydraulic fall solutions and trapped waves between successive obstructions are thoroughly investigated in §3. We finally conclude with a summary of the results and discussions on perspectives in §4.

II. FORMULATION

A. Descriptions of problem

A system composed of two superposed inviscid and incompressible fluids separated by a massless elastic plate is considered in two-dimensional space. The fluid in each layer has a finite depth and a constant density. The heavier fluid with density ρ_1 occupies the lower layer, whose properties are designated with subscript 1. Meanwhile, the lighter fluid with density ρ_2 occupies the upper layer, and its properties are analogously assigned with subscript 2. Flows in both layers are assumed to be irrotational. The system is bounded above and below both by rigid walls of infinite horizontal extent, and the change in bottom topography is locally confined (see a sketch in Fig. 1). We introduce a Cartesian coordinate system such that the x-axis is parallel to the flat top wall and the y-axis is in the opposite direction of gravity. At infinity, the velocities denoted by U_j upstream (and likewise by V_j downstream, $j=1,2$) are uniform, and the depth of each layer

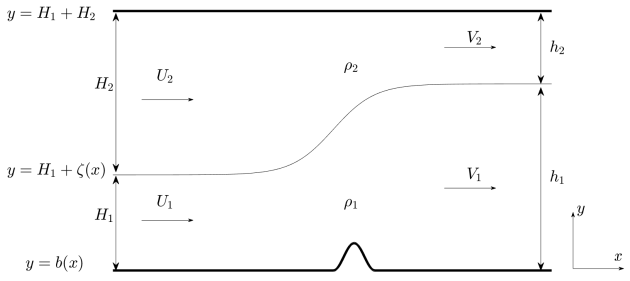

Figure 1. Sketch of two-layer channel flow past an obstacle at the bottom. The fluids are separated by a thin, massless elastic plate modeled as a hyperelastic shell.

marked by H_j upstream (and correspondingly by h_j downstream) is constant. Then the upper boundary is represented by $y=H_1+H_2=h_1+h_2$, the bottom topography is expressed as $y=b(x)$, and the interface is designated $y=H_1+\zeta(x)$. The massless elastic plate of flexural rigidity D is assumed to have negligible thickness and is modeled according to the special Cosserat theory of hyperelastic shells (see Ref. 44).

The velocity potential functions denoted as ϕ_j are introduced, which satisfy the governing equations of irrotational motion

$$\begin{aligned} &\phi_{1xx}+\phi_{1yy}=0\,, \qquad \text{for} \quad b(x)<y<H_1+\zeta(x)\,,\\ &\phi_{2xx}+\phi_{2yy}=0\,, \qquad \text{for} \quad H_1+\zeta(x)<y<H_1+H_2\,. \end{aligned} \tag{1}$$

The impermeability conditions at the top and bottom walls are written as

$$\begin{aligned} 0&=\phi_{2y}\,, \qquad \text{at} \quad y=H_1+H_2\,,\\ \phi_{1x}b_x&=\phi_{1y}\,, \qquad \text{at} \quad y=b(x)\,. \end{aligned} \tag{2}$$

For steady states, the kinematic boundary conditions at the interface can be written as

$$0=\phi_{1y}-\phi_{1x}\zeta_x=\phi_{2y}-\phi_{2x}\zeta_x\,, \qquad \text{at} \quad y=H_1+\zeta(x)\,, \tag{3}$$

which means the normal velocity is continuous across the elastic plate. Using the Bernoulli constant at infinity, the continuity of pressure across the interface leads to the dynamic boundary condition

$$\begin{aligned} &\frac{1}{2}\left[\rho_1\left(\phi_{1x}^2+\phi_{1y}^2\right)-\rho_2\left(\phi_{2x}^2+\phi_{2y}^2\right)\right]+\frac{D}{2}\left(2\kappa_{ss}+\kappa^3\right)\\ &+g\zeta(\rho_1-\rho_2)-\frac{1}{2}\left(\rho_1U_1^2-\rho_2U_2^2\right)=0\,, \end{aligned} \tag{4}$$

where κ is the curvature of the interface and s is the arclength parameter. We remark that the special Cosserat theory is applied here, and this nonlinear elastic model was first proposed by Toland[44]. The explicit expression of κ in the Cartesian coordinate system can be written as $\kappa=\frac{\zeta_{xx}}{\left(1+\zeta_x^2\right)^{3/2}}$. In addition, the conservation of mass leads to

$$U_1H_1=V_1h_1\,, \qquad U_2H_2=V_2h_2\,. \tag{5}$$

Equations (1)-(5) form a closed system for the problem of interfacial hydroelastic hydraulic falls. Finally, for the clarity and convenience of discussion, we introduce property ratios

$$\begin{aligned} R &= \frac{\rho_2}{\rho_1}, \qquad \Theta = \frac{H_2}{H_1}, \\ \beta &= \frac{U_2}{U_1}, \qquad \beta_1 = \frac{V_1}{U_1}, \qquad \beta_2 = \frac{V_2}{U_2}, \end{aligned} \tag{6}$$

where R is the density ratio, Θ is the depth ratio, and β, β_1, β_2 are velocity ratios. The upstream and downstream Froude numbers are defined as

$$\begin{aligned} F_{1u} &= \frac{U_1}{\sqrt{gH_1}}, \qquad F_{2u} = \frac{U_2}{\sqrt{gH_2}}, \\ F_{1d} &= \frac{V_1}{\sqrt{gh_1}}, \qquad F_{2d} = \frac{V_2}{\sqrt{gh_2}}. \end{aligned} \tag{7}$$

Finally, the dimensionless parameter describing the flexural rigidity reads $E_b = \frac{D}{\rho_1 g H_1^4}$.

B. Linear analysis

In the following section, we explore the linear theory of this model. The whole system is disturbed around the trivial solution $\phi_j = U_j x$ and $\zeta = 0$ under the smallness assumption on wave amplitude and bottom topography, *i.e.*, $\zeta/H_1 \sim \mathcal{O}(\varepsilon)$ and $b/H_1 \sim \mathcal{O}(\varepsilon^2)$, where $\varepsilon \ll 1$ is introduced as a small parameter. By considering perturbations of the form $\mathrm{e}^{\mathrm{i}kx}$, we can drop the nonlinear terms in Eqs. (1)-(5), and after some algebra, derive the linear solutions and the dispersion relations. One first obtains

$$\begin{aligned} \zeta &= \varepsilon \frac{\alpha}{\mathrm{i}U_1} \sinh(kH_1)\mathrm{e}^{\mathrm{i}kx}, \\ \phi_1 &= U_1 x + \varepsilon\alpha \cosh(ky)\mathrm{e}^{\mathrm{i}kx}, \\ \phi_2 &= U_2 x - \varepsilon\alpha\beta \frac{\sinh(kH_1)}{\sinh(kH_2)} \cosh(kH_1 + kH_2 - ky)\mathrm{e}^{\mathrm{i}kx}. \end{aligned} \tag{8}$$

Similar derivation can be applied to the quantities downstream. Then, substituting the expressions of ϕ_j and ζ into the linearized dynamic boundary condition (4) yields the linear dispersion relations

$$\begin{aligned} F_{1u}^2 &= \frac{(1 - R + K^4 E_b)\tanh(K)\tanh(\Theta K)}{K\tanh(\Theta K) + R\beta^2 K\tanh(K)}, \\ F_{1d}^2 &= \frac{(1 - R + K^4 E_b)\tanh\left(\frac{K}{\beta_1}\right)\tanh\left(\frac{\Theta K}{\beta_2}\right)}{\frac{K}{\beta_1}\tanh\left(\frac{\Theta K}{\beta_2}\right) + R\beta^2 \frac{\beta_2^2}{\beta_1^3} K\tanh\left(\frac{K}{\beta_1}\right)}, \end{aligned} \tag{9}$$

where $K = kH_1$ is the normalized wavenumber. In later discussions, these linear dispersion relations will be used to predict the wavelength of trapped waves for the flow past two successive obstacles. It is worth noting that the parameter E_b shows up, representing the effect of hydroelasticity. The fourth-order derivative in the Cosserat theory leads to the additional term K^4, which changes the behavior of linear dispersion relations (shown later in section §3). Similar to the dispersion relation of single-layer flexural-gravity waves, there is always a point at which the phase velocity is equal to the group velocity, which occurs at the minimum of the Froude number. With an upstream Froude number below this minimum, there exist no waves. The dimensionless wavenumber at which F_{1u} reaches the minimum is denoted by K_{min}. In the vicinity of K_{min}, the wavenumber predicted by linear theory might no longer adapt, and nonlinear analysis is therefore necessary. As we can see in Ref. 24, at K_{min}, nonlinear analysis shows that no solitary waves exist. Moreover, even if the obstruction on bottom topography is not present in linear dispersion relations, it influences the Froude numbers by varying the parameter β_1 or β_2. We remark that β_1 and β_2 are related through the conservation of the fluid in the far field with Θ and β fixed. As a result, with different obstructions, *i.e.*, other β_1 values, the linear dispersion relation for F_{1d} changes while the one for F_{1u} remains the same. The critical Froude number for the lower fluid upstream is defined by taking the limit $K \to 0$, and we have $F_{1u}^{*\,2} = \frac{\Theta(1-R)}{\Theta + R\beta^2}$.

C. Weakly nonlinear analysis

In this part, weakly nonlinear analysis is performed, assuming that the thickness of both layers is small compared to the horizontal characteristic wavelength. The characteristic wavelength is denoted by l, and the typical amplitude of interfacial waves is designated as a. Small parameters $\varepsilon = a/H_1$ and $\mu^2 = (H_1/l)^2$ are defined with $\varepsilon = \mu^2$ to balance the dispersion and nonlinearity. Boussinesq scaling is applied for nondimensionalization:

$$\begin{aligned} &x = lx', \quad y = H_1 y', \quad \zeta = a\zeta', \\ &b = \varepsilon^2 H_1 b', \quad \phi_j = \sqrt{gH_1}F_{1u} l x' + \frac{agl}{\sqrt{gH_1}}\phi_j'. \end{aligned} \tag{10}$$

Notably, the obstruction is assumed to be $b \sim \varepsilon^2 H_1$, and the velocity potentials are separated into two parts: a background flow and its perturbation. We will show that the flexural effects only exist in the higher order terms in the forced KdV-type model unless the parameter E_b has a significant value so that $E_b \sim \varepsilon^{-1}$.

Dropping the apostrophes of dimensionless variables, the field and boundary equations can then be expressed as

$$\begin{aligned} &\varepsilon\phi_{1xx} + \phi_{1yy} = 0, \quad \text{for } 0 < y < 1 + \varepsilon\zeta, \\ &\varepsilon\phi_{2xx} + \phi_{2yy} = 0, \quad \text{for } 1 + \varepsilon\zeta < y < 1 + \Theta, \\ &\phi_{1y} = \varepsilon^2 F_{1u} b_x + \varepsilon^3 \phi_{1x} b_x \quad \text{at } y = \varepsilon^2 b, \\ &\phi_{2y} = 0, \quad \text{at } y = 1 + \Theta. \end{aligned} \tag{11}$$

The kinematic conditions at $y = 1 + \varepsilon\zeta$ are recast to

$$\begin{aligned} \phi_{1y} &= \varepsilon F_{1u}\zeta_x + \varepsilon^2 \phi_{1x}\zeta_x, \\ \phi_{2y} &= \varepsilon F_{1u}\zeta_x + \varepsilon^2 \phi_{2x}\zeta_x. \end{aligned} \tag{12}$$

We remark that the governing equations, the boundary conditions, and the kinematic conditions at the interface presented above are the same as the two-layer pure gravity case in Ref.

46. However, the dynamic condition at the interface becomes different as the hydroelastic term is involved:

$$\zeta(1-R)+F_{1u}\phi_{1x}-R\beta F_{1u}\phi_{2x}+\frac{1}{2}(\phi_{1y}^2-R\phi_{2y}^2) +\frac{\varepsilon}{2}(\phi_{1x}^2-R\phi_{2x}^2)+\varepsilon^2 E_b\zeta_{xxxx}=0. \tag{13}$$

Substituting the asymptotic expansions of velocity potentials up to $\mathscr{O}(\varepsilon^3)$ satisfying Eq. (11) into the kinematic and dynamic conditions (Eqs. 12 and 13) yields three equations. Solvability of the first-order problem indicates that $F_{1u}=F_{1u}^*+\varepsilon\lambda$. More details of this procedure can be referred to Refs. 13 and 46. After some algebra, one single equation retaining the terms valid up to $\mathscr{O}(\varepsilon)$ writes

$$b_x-\frac{2\lambda}{F_{1u}^*}\frac{\Theta+R\beta^2}{\Theta}\zeta_x+\frac{1}{3}(1+\Theta R\beta^2)\zeta_{xxx}+3\left(1-\frac{R\beta^2}{\Theta}\right)\zeta\zeta_x +\varepsilon\left[\mathscr{F}(b,\zeta)+\mathscr{S}(b,\zeta)+E_b\zeta_{xxxxx}\right]=0, \tag{14}$$

where $\mathscr{F}(b,\zeta)$ contains terms related to b_x, ζ_x, ζ_{xxx}, and $\zeta\zeta_x$, appearing in the traditional forced Korteweg de-Vries (fKdV) equation, and $\mathscr{S}(b,\zeta)$ includes terms associated with b_{xxx}, $b\zeta$, $\zeta_x\zeta_{xx}$, $\zeta\zeta_{xxx}$, and $\zeta^2\zeta_x$, presenting in the general form of the forced fifth-order KdV equation along with ζ_{xxxxx}.

In Eq. (14), at $\mathscr{O}(1)$, the forced KdV equation in the pure gravity case is recovered. The flexural effects only appear in the next-to-leading order ($\mathscr{O}(\varepsilon)$). As a result, unless the rigidity parameter is large enough ($E_b\sim\varepsilon^{-1}$), the higher order of the dispersive term will not be found in the leading order.

D. Numerical scheme

The fully nonlinear problem is numerically solved using the boundary integral equation method with the arclength parameterization of the interface. This scheme was first proposed by Forbes and Schwartz in Ref. 20 and is widely used to solve the steady solutions of nonlinear water-wave problems with a free surface. The numerical scheme will be briefly introduced, and more details are referred to Refs. 5, 16, and 20. H_1 and H_1U_1 are the units of length and velocity potential for non-dimensionalization. The fluid interface is first parametrized by

$$x=X(s)\,,\qquad y=\zeta(x)+1=Y(s)\,, \tag{15}$$

so that the parametric equation is satisfied on the interface:

$$\left(\frac{dX}{ds}\right)^2+\left(\frac{dY}{ds}\right)^2=1\,. \tag{16}$$

The dynamic boundary condition (4) is then rewritten as

$$\frac{1}{2}\left(\phi_1'^2-R\phi_2'^2\right)-\frac{1}{2}(1-R\beta^2)+\frac{1}{F_{1u}^2}(1-R)(Y(s)-1) +\frac{E_b}{F_{1u}^2}\left(k''+\frac{1}{2}k^3\right)=0\,, \tag{17}$$

where $\kappa=Y''X'-X''Y'$ is the parameterized curvature of the interface, and the prime denotes differentiation with respect to the arclength parameter s.

Following Belward and Forbes[5], Cauchy's integral formula is applied to the complex velocity potential $w_j(z)=\phi_j(x,y)+\mathrm{i}\psi_j(x,y)$ for both upper and lower layers, where $z=x+\mathrm{i}y$ is the independent complex variable and ψ_j is the stream function. Thus, the complex velocity can be defined as

$$\chi_j=\begin{cases}\dfrac{dw_j}{dz}-1=\phi_{jx}-\mathrm{i}\phi_{jy}-1, & j=1\,,\\[2mm] \dfrac{dw_j}{dz}-\beta=\phi_{jx}-\mathrm{i}\phi_{jy}-\beta, & j=2\,.\end{cases} \tag{18}$$

For the lower layer, the integration path is shown in Fig. 2(a), which consists of the interface, channel bottom, and vertical lines joining them at $x=\pm L$ and $L\to\infty$. Since we focus on the hydraulic fall solutions which approach constant states on both sides at infinity in the present work, the numerical computations can only be performed in a truncated domain, and the truncation error is taken into account in integration. On the other side, the integration path for the upper fluid is shown in Fig. 2(b) with a modification to avoid setting mesh points on the top wall since we are only interested in the values on the interface. A symmetric extension is applied to satisfy the impermeability boundary condition. Denoting the velocity potential at the interface by Φ_j and the horizontal velocity at the channel bottom by u, the Cauchy integral formula gives

$$\pi(\Phi_1'X'(s)-1)=\int_{-\infty}^{\infty}\frac{(\Phi_1'(\hat\sigma)-X'(\hat\sigma))(Y(\hat\sigma)-Y(s))+Y'(\hat\sigma)(X(\hat\sigma)-X(s))}{(X(\hat\sigma)-X(s))^2+(Y(\hat\sigma)-Y(s))^2}d\hat\sigma -\int_{-\infty}^{\infty}\frac{(u(\hat\sigma)(1+b_x(\hat\sigma)^2)-1)(b(\hat\sigma)-Y(s))+b_x(\hat\sigma)(\hat\sigma-X(s))}{(\hat\sigma-X(s))^2+(b(\hat\sigma)-Y(s))^2}d\hat\sigma\,, \tag{19}$$

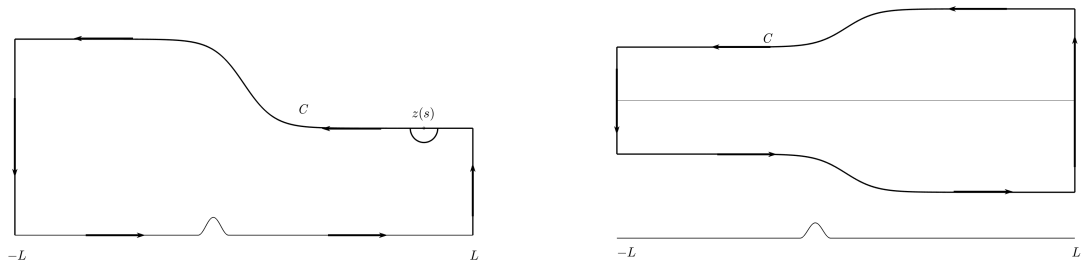

(a) (b)

Figure 2. Sketch of integration paths: (a) integration path of the lower fluid; (b) integration path of the upper fluid.

$$\begin{aligned}\pi(u(x)-1) = &\int_{-\infty}^{\infty} \frac{(\Phi_1'(\hat{\sigma})-X'(\hat{\sigma}))(Y(\hat{\sigma})-b(x))+Y'(\hat{\sigma})(X(\hat{\sigma})-x)}{(X(\hat{\sigma})-x)^2+(Y(\hat{\sigma})-b(x))^2}d\hat{\sigma}\\ &-\int_{-\infty}^{\infty} \frac{(u(\hat{\sigma})(1+b_x(\hat{\sigma})^2)-1)(b(\hat{\sigma})-b(x))+b_x(\hat{\sigma})(\hat{\sigma}-x)}{(\hat{\sigma}-x)^2+(b(\hat{\sigma})-b(x))^2}d\hat{\sigma}\,,\end{aligned} \tag{20}$$

and

$$\begin{aligned}\pi(\Phi_2'X'(s)-\beta) = &\int_{-\infty}^{\infty} \frac{-(\Phi_2'(\hat{\sigma})-\beta X'(\hat{\sigma}))(Y(\hat{\sigma})-Y(s))-\beta Y'(\hat{\sigma})(X(\hat{\sigma})-X(s))}{(X(\hat{\sigma})-X(s))^2+(Y(\hat{\sigma})-Y(s))^2}d\hat{\sigma}\\ &-\int_{-\infty}^{\infty} \frac{-(\Phi_2'(\hat{\sigma})-\beta X'(\hat{\sigma}))(2+2D-Y(\hat{\sigma})-Y(s))-\beta Y'(\hat{\sigma})(X(\hat{\sigma})-X(s))}{(X(\hat{\sigma})-X(s))^2+(2+2\Theta-Y(\hat{\sigma})-Y(s))^2}d\hat{\sigma}\,,\end{aligned} \tag{21}$$

where $\hat{\sigma}$ represents the value of arclength at the varying point on the path, the evaluation point s is placed on the interface and x on the bottom.

The mesh grids on which the corresponding unknowns $(\Phi_1', \Phi_2', X', Y')$ need to be solved are equally distributed on the interface and on the bottom, denoted respectively as s_j $(j = 1, ..., M)$ and x_j $(j = 1, ..., N)$. The other two sets of mesh grids, defined as middle points,

$$\begin{aligned} s_j^m &= \frac{s_j + s_{j+1}}{2}, \qquad j = 1, 2, ..., M-1\,,\\ x_j^m &= \frac{x_j + x_{j+1}}{2}, \qquad j = 1, 2, ..., N-1\,,\end{aligned} \tag{22}$$

are introduced to avoid the singularities in the computations of the Cauchy integrals. Different grid sizes have been applied to verify the grid convergence and to find the appropriate spacing ensuring the computation accuracy: $(ds, dx) = (s_{j+1} - s_j, x_{j+1} - x_j) = (0.05, 0.1), (0.1, 0.2), (0.2, 0.4)$. Low resolution $(ds, dx) = (0.2, 0.4)$ can lead to the divergence of Newton's iterative method. The convergence is obtained with $(ds, dx) = (0.1, 0.2)$, and increasing the resolution of mesh grids does not contribute to an apparent change in wave profile. The domain size is decided by (M, N) with a fixed mesh resolution. Test cases with $(M, N) = (401, 201), (601, 301), (801, 401)$ are performed to ensure that the influence of domain length on wave profile can be ignored. In the present paper, the settings $(ds, dx) = (0.1, 0.2)$ and $(M, N) = (401, 201), (601, 301)$ are used for numerical simulations.

Boundary conditions and conservation of the total fluid height in the far-field give additional equations

$$1 + \Theta = \frac{1}{\beta_1} + \frac{\Theta}{\beta_2}\,, \qquad \beta_1 = \frac{1}{Y(s_M)}\,, \tag{23}$$

substituting which into the dynamic boundary condition yields

$$\frac{1}{2}F_{1u}^2 R\beta^2\left(1-\beta_2^2\right) + \frac{1}{2}F_{1u}^2\left(\beta_1^2 - 1\right) + (1-R)\left(\frac{1}{\beta_1} - 1\right) = 0\,. \tag{24}$$

F_{1u}, β_1, and β_2 are thus solved as part of the solution. To solve the whole system formed by the Cauchy integral equations (19)-(21), the parameterized dynamic boundary condition (24), and the parametric equation (16), we need three more equations for the Newton iteration. These equations can vary with the form of solution to be found or be decided according to the convergence of the solution in iteration. Note that these additional equations can make the numerical sim-

ulations diverge even if they have reasonable forms. For example, $Y'(1)=0, u'(1)=1$ and $\Phi_2'(1)=\beta$ are used for hydraulic fall solutions (see Refs. 15, 16, and 46). Other typical conditions can also be chosen as $Y'(1)=0, Y'(2)=0$ and $Y'(M-1)=0$, used in the present work, so that the far-field condition can be approximately satisfied.

III. RESULTS

Following Refs. 34, 35, and 46, the bottom topography features a combination of separated half-period cosine-type profiles. Specifically, $b(x)$ can be defined as

$$b(x)=\begin{cases} A_1\cos^2\left(\dfrac{\pi(x-x_1)}{L_1}\right), & -\dfrac{L_1}{2}<x-x_1<\dfrac{L_1}{2}, \\ A_2\cos^2\left(\dfrac{\pi(x-x_2)}{L_2}\right), & -\dfrac{L_2}{2}<x-x_2<\dfrac{L_2}{2}, \\ 0, & |x-x_1|>\dfrac{L_1}{2}, |x-x_2|>\dfrac{L_2}{2}, \end{cases}$$

where A_j and L_j are the height and width of the obstacle, respectively. Two obstacles are centered at $x=x_1$ and $x=x_2$. The obstacle's height may be positive or negative, corresponding to convex and concave. We remark that no solutions considered in this paper have A_1 and A_2 equal to zero (*i.e.*, there is always bottom topography).

From the weakly nonlinear analysis in §2, the hydroelasticity only adds a fifth-order derivative term to the higher-order part and some characteristics of the lower-order equations are preserved. The analyses of the low-order equations, *i.e.*, the fKdV equation and the modified fKdV equation, are similar to those in Ref. 46, where pure gravity interfacial hydraulic falls can be divided into six regimes in line with the upstream Froude number and depth ratio. For example, the sign of the quadratic nonlinear term depends on $\Theta-\sqrt{\beta^2 R}$, which determines the elevation or depression of the downstream level of the interface. With the upstream flow chosen to be subcritical with $F_{1u}<F_{1u}^*$, only three regimes considered here can be defined, namely (I) 'thick upper layer' for $\Theta>\sqrt{\beta^2 R}$, (II) 'thick bottom layer' for $\Theta<\sqrt{\beta^2 R}$, and (III) the critical case for $\Theta=\sqrt{\beta^2 R}$. We remark that the elevation or depression of the downstream level in critical case depends on the convexity-concavity property of the bottom topography. In this paper, the parameter β is fixed as $\beta=1$, and the density ratio is specified as $R=0.6$. We select the depth ratio $\Theta=2$ for thick upper layer cases and $\Theta=0.5$ for thick bottom layer cases. Thus, the critical upstream Froude numbers can be fixed as $F_{1u}^*=0.55$, 0.43, and 0.475 for regimes (I), (II), and (III).

1. *Single obstacle*

We first consider the cases where $A_2=0$ so that $y=b(x)$ describes a uniform channel bottom with only one obstacle. As the initial guess is essential for Newton's iterative method, here we use the pure gravity hydraulic fall solutions found in Ref. 46 as the initial condition. We then add the hydroelasticity based on a standard numerical continuation method (namely, gradually increasing the flexural rigidity D from zero).

Considering Regime (I): subcritical flow upstream with a thick upper layer, Fig. 3 shows typical hydraulic fall profiles over a convex obstacle with different sizes and values of parameter E_b. By increasing the obstacle's height or width, the upstream Froude number decreases while the downstream Froude number increases (see Fig. 3a). This result is comparable to pure gravity interfacial hydraulic falls with subcritical flow upstream and a thick upper layer. Furthermore, it is coherent with the single layer case in the same flow regime upstream in Ref. 35 as it can be considered a particular case of a thick upper layer. Figure 3(b) shows wave profiles with different rigidity values for $E_b=0.5, 0.2, 0.1$. A slight elevation shows up right before the hydraulic fall, a similar phenomenon observed in single-layer flexural-gravity or gravity-capillary hydraulic falls. As the size of the obstacle or the value of the parameter E_b decreases, the upstream Froude number approaches the minimum of the linear dispersion relation, which means the potential of having an intersection point with the linear phase speed and hence generation of a train of waves upstream. In Fig. 3, the elevation before hydraulic fall grows with the upstream Froude number and becomes part of a decaying wave train. On the contrary, with a larger obstacle, the elevation becomes less noticeable, and the steepness of the fall is weakened. The underlying mechanism is, in fact, different: (*i*) the decrease of the size of obstruction (A_1, L_1) contributes to the increase of the upstream Froude number, and the minimum of F_{1u} given by linear dispersion relation remains invariant; (*ii*) the decrease of the rigidity parameter E_b mainly leads to a lower minimum of F_{1u} as it changes the linear dispersion relation. It is worth noting that we did not manage to find the solutions to concave obstacles in Regime (I). The main reason is that a higher upstream Froude number which might intersect with the linear dispersion relation and a small jump-up at the obstacle's position (see Ref. 46) resulting from the concavity of obstruction, can lead to long oscillatory waves upstream. To satisfy the radiation condition, which requires decaying waves upstream without energy coming from infinity, we need an extremely long domain for the solution to be physically relevant, leading to high computational costs. Solutions past a concave obstacle with a large size and a small surface tension parameter may exist according to the single-layer gravity-capillary case in Ref. 23. In this case, the capillary effects are much smaller compared with the influence of bottom topography.

It can be observed that small-amplitude spurious periodic waves may exist downstream where the flow is supercritical, in that the downstream truncation of the computation domain acts as a source of disturbance downstream. And the downstream Froude number intersects the linear dispersion curve in Fig. 4 (see also Ref. 35). As we look for steady hydraulic fall solutions, no wave should exist in the far-field downstream (otherwise, the solution becomes generalized hydraulic fall). As explained in §2, the numerical scheme considers the truncation error in the integration. These spurious waves are due

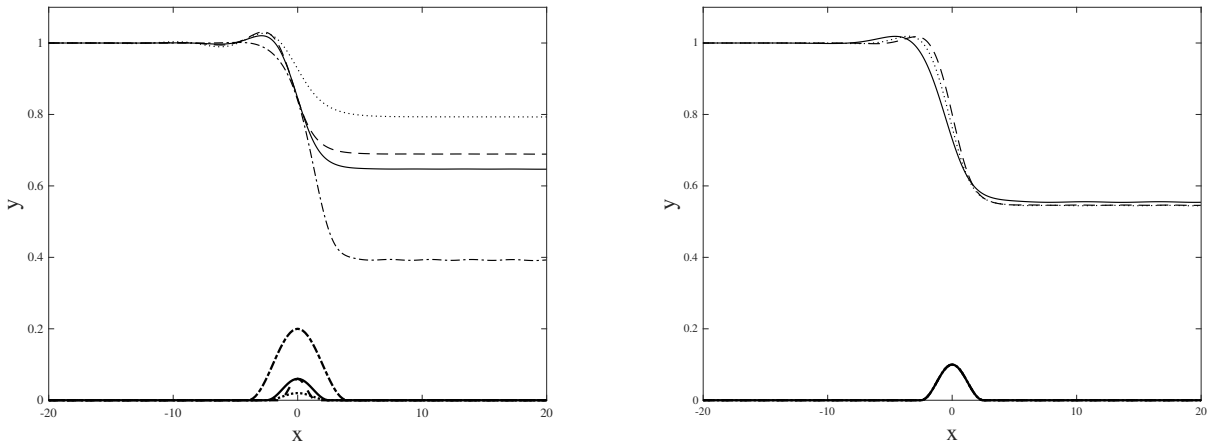

Figure 3. Interfacial hydroelastic hydraulic falls over a convex obstacle in Regime (I). (a) Wave profiles with $E_b = 0.1$ and: $(A_1, L_1, F_{1u}, F_{1d}) = (0.06, 5, 0.426, 0.819)$ (solid line); $(A_1, L_1, F_{1u}, F_{1d}) = (0.02, 5, 0.487, 0.690)$ (dotted line); $(A_1, L_1, F_{1u}, F_{1d}) = (0.06, 3, 0.445, 0.778)$ (dashed line); $(A_1, L_1, F_{1u}, F_{1d}) = (0.2, 8, 0.291, 1.183)$ (dash-dotted line). (b) Wave profiles with $A_1 = 0.1$, $L_1 = 5$, and different flexural rigidities: $(E_b, F_{1u}, F_{1d}) = (0.5, 0.381, 0.924)$ (solid line); $(E_b, F_{1u}, F_{1d}) = (0.2, 0.376, 0.936)$ (dotted line); $(E_b, F_{1u}, F_{1d}) = (0.1, 0.377, 0.935)$ (dashed line).

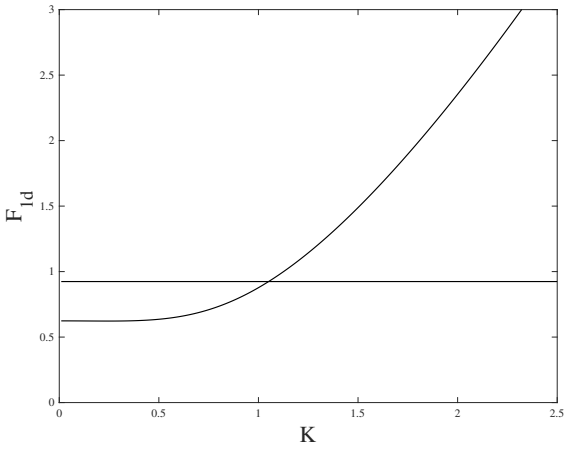

Figure 4. The downstream dispersion relation for the solid-line case of Fig. 3(b) (*i.e.*, $E_b = 0.5$). The curve is the linear dispersion relation $F_{1d}(K)$ in Eq. (9) with parameters β_1 and β_2 found by solving the fully nonlinear problem. The horizontal line corresponds to the downstream Froude number solved for the case.

to the additional equations which provide other limits on the boundary of the computational domain. Appropriate far-field conditions downstream can be applied to reduce the amplitude of the spurious waves so that the wave amplitude becomes negligible and the solutions become physically relevant. For example, $Y'(M) = 0$ instead of $Y'(M-1) = 0$ might give rise to more obvious oscillations downstream.

The solution branches in the $F - E_b$ plane for $0.1 < E_b < 5$ with different geometrical parameters of the submerged obstacle ($A_1 = 0.06, 0.1, 0.16$) are plotted in Fig. 5(a). These curves are obtained by varying the value of parameter E_b and solving for the Froude number (equivalently the interfacial wave solution), which is a function of E_b with other parameters fixed. Overall, the upstream Froude number augments, and the downstream Froude number decreases, along with the growth of the parameter E_b. The opposite trend of variation for upstream and downstream Froude numbers has been found as a prominent feature in the pure gravity case for the same regime. However, the interpretation of the upstream and downstream Froude numbers is not monotone due to the additional flexural effects. The existence of turning points shows that the solution is not unique for a critical range of the Froude numbers. For example, the solution branch with $(A_1, L_1) = (0.1, 5)$ has a turning point $E_b^* \in (0.1, 0.2)$ (see the dotted line in Fig. 5a). The corresponding solutions with $E_b = 0.1$ and $E_b = 0.22$, which have the same Froude number, are shown in Fig. 5(b). Similarly, the solution branch shows two turning points near the bifurcation point with $(A_1, L_1) = (0.16, 5)$. An example of solutions having the same Froude number is also given in Fig. 5(b), with $E_b = 0.68, 0.38, 0.221$. We remark that the phenomenon discussed here is not bistability in the traditional case as the difference of E_b represents a different rigidity, lower depth upstream, or equivalently different fluid speed. The linear dispersion relations in Eq. (9) can explain the existence of multiple solutions. The introduction of the rigidity parameter allows for dispersion curves for the same Froude number, which gives rise to various solutions. A similar analysis for the single-layer gravity-capillary case can be found in Ref. 39.

Interfacial hydraulic falls in Regime (II), *i.e.*, subcritical flow upstream with a thick bottom layer, with a concave obstacle, are shown in Fig. 6. These wave profiles present a more significant depth of the lower fluid downstream and a smaller

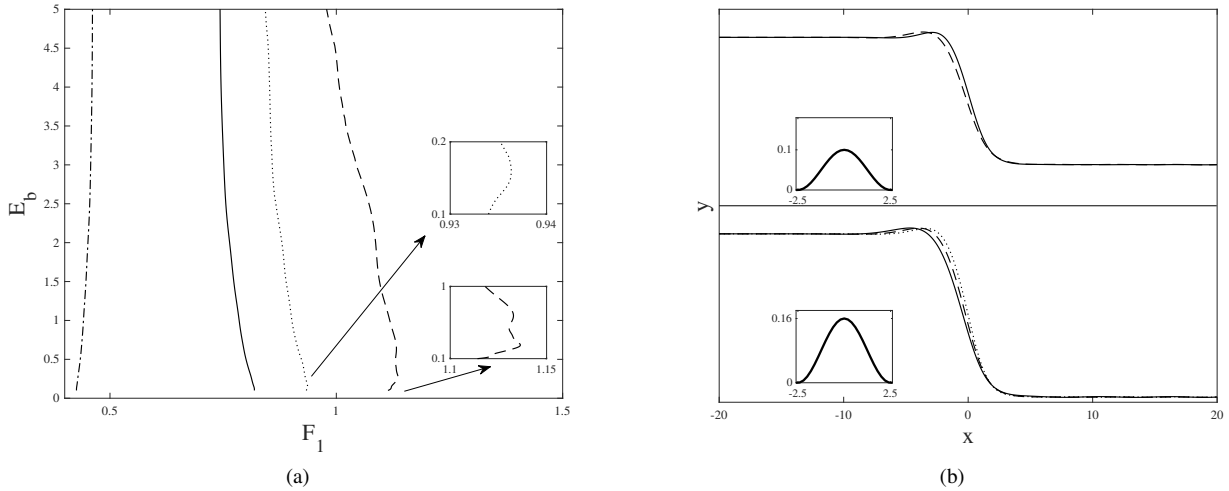

(a) (b)

Figure 5. (a) Downstream solution branches in the $F_1 - E_b$ plane for hydraulic falls over a convex obstacle in Regime (I). The obstruction is characterized by: $(A_1, L_1) = (0.06, 5)$ (solid line); $(A_1, L_1) = (0.1, 5)$ (dotted line); $(A_1, L_1) = (0.16, 5)$ (dashed line). Upstream solution branch for $(A_1, L_1) = (0.06, 5)$ (dash-dotted line) is presented for comparison. (b) Hydraulic fall profiles for the same Froude number and different values of E_b. Top: $(A_1, L_1, F_{1u}, F_{1d}) = (0.1, 5, 0.377, 0.934)$ with $E_b = 0.1$ (solid line) and $E_b = 0.22$ (dashed line); Bottom: $(A_1, L_1, F_{1u}, F_{1d}) = (0.16, 5, 0.307, 1.132)$ with $E_b = 0.68$ (solid line), $E_b = 0.38$ (dashed line), and $E_b = 0.221$ (dotted line).

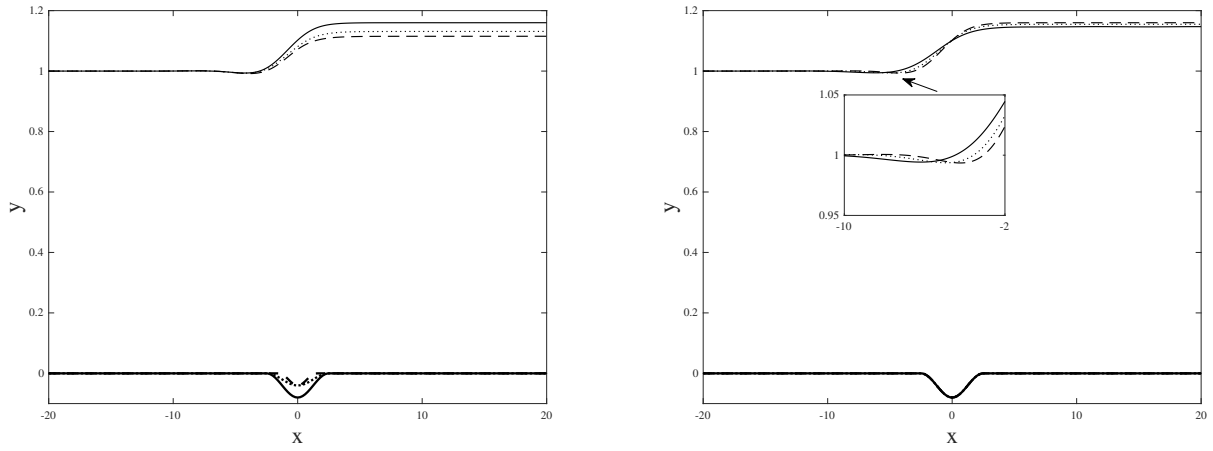

(a) (b)

Figure 6. Interfacial hydroelastic hydraulic falls over a concave obstacle in Regime (II). (a) Wave profiles with $E_b = 0.1$ and: $(A_1, L_1, F_{1u}, F_{1d}) = (-0.08, 5, 0.366, 0.293)$ (solid line); $(A_1, L_1, F_{1u}, F_{1d}) = (-0.04, 5, 0.381, 0.317)$ (dotted line); $(A_1, L_1, F_{1u}, F_{1d}) = (-0.04, 3, 0.389, 0.330)$ (dashed line). (b) Wave profiles with $A_1 = -0.08$, $L_1 = 5$, and different flexural rigidities: $(E_b, F_{1u}, F_{1d}) = (0.5, 0.373, 0.304)$ (solid line); $(E_b, F_{1u}, F_{1d}) = (0.2, 0.369, 0.297)$ (dotted line); $(E_b, F_{1u}, F_{1d}) = (0.1, 0.366, 0.293)$ (dashed line).

downstream Froude number than upstream. We remark that the flow downstream is still supercritical as $F_{1d} > F^*_{1d}$. With larger values of the parameters $|A_1|$ and L_1, the lower layer ultimately reaches a higher level downstream, and the difference between the Froude numbers upstream and downstream becomes larger. In the same vein, by decreasing the size of the obstacle or the value of E_b, the small depression right before the fall becomes more apparent, and a train of decaying waves exists upstream. Thus for the same reason explained for Regime (I), we only consider the concave obstacle here.

Solution branches in the $F - E_b$ plane presented in Fig. 7 demonstrate similar trends in general: the upstream and downstream Froude numbers increase with the parameter E_b. However, unlike the result of Regime (I), the variation trend is monotone, and there are no turning points in the three cases shown in Fig. 7.

The results of Regime (III) - subcritical flow upstream with a critical depth - over a convex or a concave obstacle are presented in Figs. 8 and 9. The convex obstacle leads to 'jump-downs'. In contrast, the concave obstacle leads to 'jump-ups'.

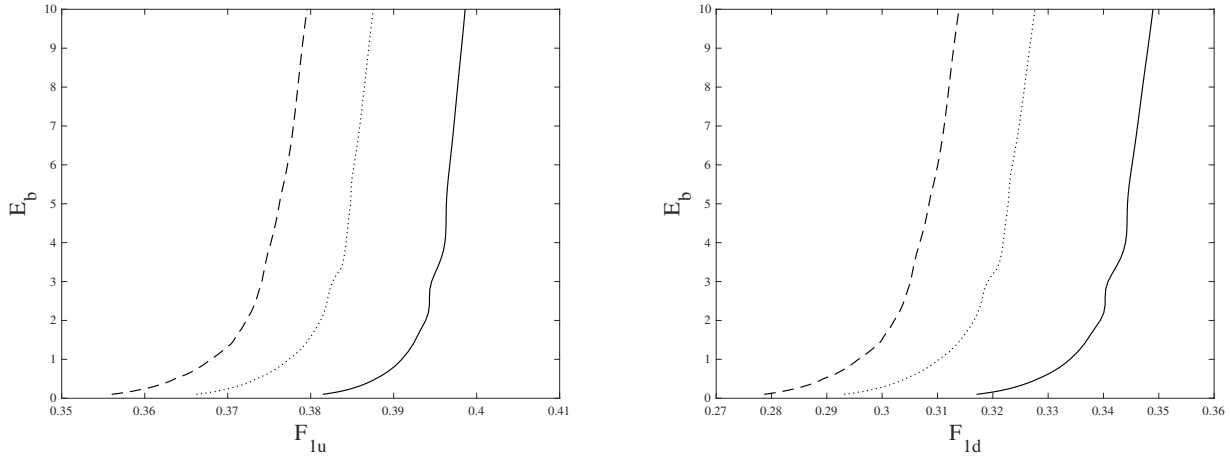

(a) (b)

Figure 7. Solution branches in the $F_1 - E_b$ plane for hydraulic falls over a concave obstacle in Regime (II). The obstruction is characterized by: $(A_1, L_1) = (-0.04, 5)$ (solid line); $(A_1, L_1) = (-0.08, 5)$ (dotted line); $(A_1, L_1) = (-0.12, 5)$ (dashed line). (a) Upstream solution branches. (b) Downstream solution branches.

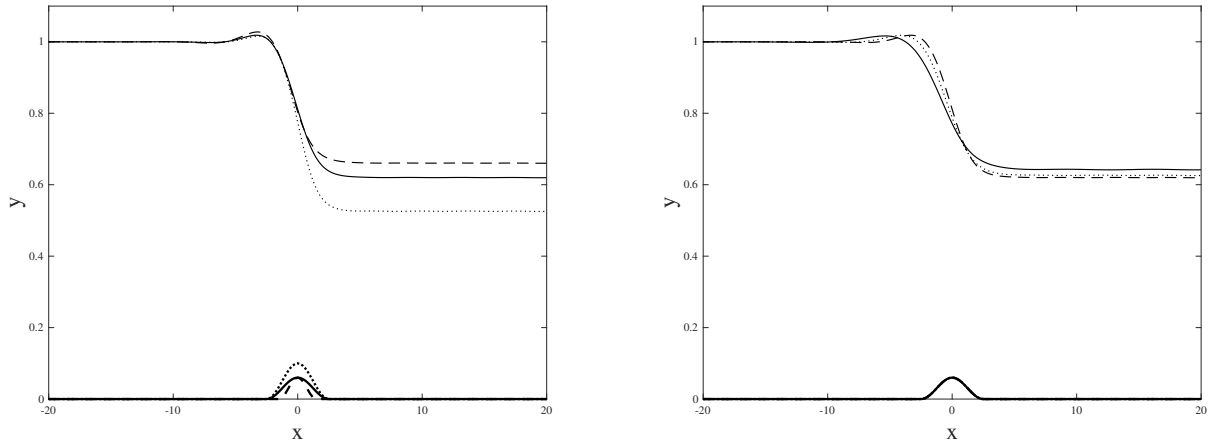

(a) (b)

Figure 8. Interfacial hydroelastic hydraulic falls over a convex obstacle in Regime (III). (a) Wave profiles with $E_b = 0.1$ and: $(A_1, L_1, F_{1u}, F_{1d}) = (0.06, 5, 0.397, 0.813)$ (solid line); $(A_1, L_1, F_{1u}, F_{1d}) = (0.1, 5, 0.356, 0.936)$ (dotted line); $(A_1, L_1, F_{1u}, F_{1d}) = (0.06, 3, 0.412, 0.767)$ (dashed line). (b) Wave profiles with $A_1 = 0.06$, $L_1 = 5$, and various flexural rigidities: $(E_b, F_{1u}, F_{1d}) = (0.5, 0.405, 0.788)$ (solid line); $(E_b, F_{1u}, F_{1d}) = (0.2, 0.399, 0.806)$ (dotted line); $(E_b, F_{1u}, F_{1d}) = (0.1, 0.397, 0.813)$ (dashed line).

In both cases, the jump condition decided by the forcing term must be satisfied by the upstream flow. Figure 8 shows that the behavior of hydraulic falls over a convex obstacle is similar to Regime (I) for various parameters of the obstruction. Moreover, bifurcation branches in the $F - E_b$ plane akin to Regime (I) are shown in Fig. 10(a). On the other side, hydraulic falls over a concave obstacle have similar behavior and bifurcation profiles to Regime (II) (see Figs. 9 and 10b). We also remark that turning points E_b^* may appear on the bifurcation curve if the size of the obstacle increases.

2. *Two successive obstacles*

In this section, we consider the effect of adding a second obstacle to the bottom topography. The convexity-concavity property of this additionally introduced obstacle can be arbitrary. For clarity, we reaffirm that the direction of fluid motion is from left to right, and the first obstruction is always placed at the origin ($x_1 = 0$). We elucidate the position of the second obstacle: being placed upstream (respectively, downstream) means on the left (respectively, right) of the first obstruction. We search for solutions characterized by a train of trapped waves between two obstacles while the hydraulic fall induced

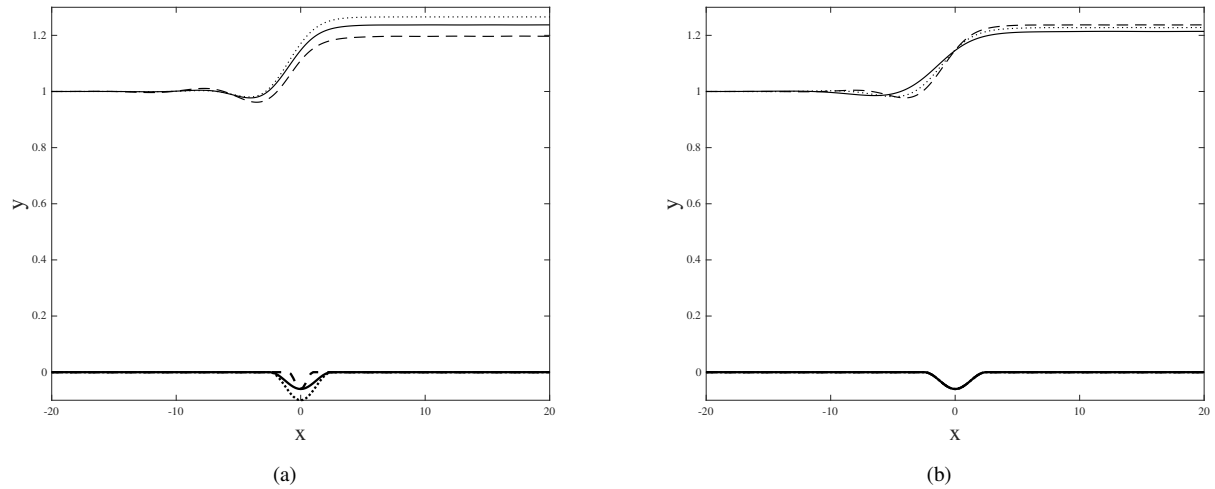

Figure 9. Interfacial hydroelastic hydraulic falls over a concave obstacle in Regime (III). (a) Wave profiles with $E_b = 0.1$ and: $(A_1, L_1, F_{1u}, F_{1d}) = (-0.06, 5, 0.437, 0.318)$ (solid line); $(A_1, L_1, F_{1u}, F_{1d}) = (-0.1, 5, 0.427, 0.300)$ (dotted line); $(A_1, L_1, F_{1u}, F_{1d}) = (-0.06, 2, 0.449, 0.343)$ (dashed line). (b) Wave profiles with $A_1 = 0.06$, $L_1 = 5$, and various flexural rigidities: $(E_b, F_{1u}, F_{1d}) = (0.5, 0.444, 0.332)$ (solid line); $(E_b, F_{1u}, F_{1d}) = (0.2, 0.440, 0.323)$ (dotted line); $(E_b, F_{1u}, F_{1d}) = (0.1, 0.437, 0.318)$ (dashed line).

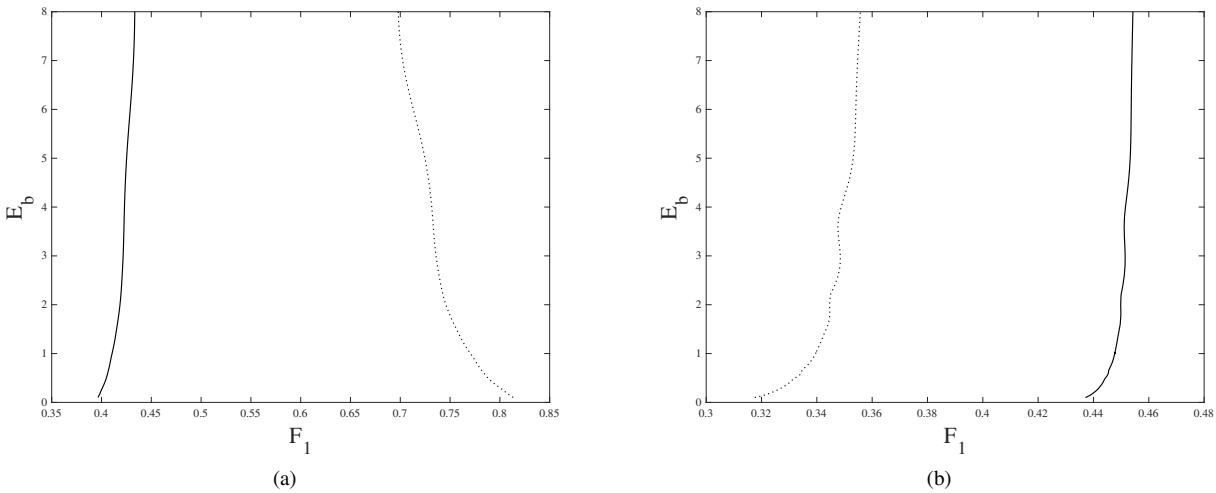

Figure 10. Solution branches in the $F_1 - E_b$ plane for hydraulic falls over one obstacle in Regime (III). (a) The obstruction is characterized by $(A_1, L_1) = (0.06, 5)$: upstream (solid line); downstream (dotted line). (b) The obstruction is characterized by $(A_1, L_1) = (-0.06, 5)$: upstream (solid line); downstream (dotted line).

by the first obstruction is retained. Consequently, the same numerical method is used and the hydraulic fall solutions computed in the precedent section are used as the initial guess. The intersection between the Froude number and the linear dispersion relation is a necessary condition for the generation of trapped waves. In the pure gravity case, the second obstacle should be placed upstream to produce trapped waves (see Ref. 46) when the upstream flow is subcritical. In the presence of an elastic sheet, unless the size of the first obstacle and the rigidity is small enough so that the upstream Froude number might intersect with the linear dispersion relation, a train of trapped waves only exist when the obstacle is added downstream. In this paper, we place the additional obstacle downstream.

Typical profiles in Regime (I) with an additional convex obstacle centered at $x_2 = 20$ and an additional concave obstacle centered at $x_2 = 15$ are shown in Figs. 11(a) and 11(b), respectively. Trapped waves exist between two submerged obstacles with a higher wave crest over the second convex obstacle (see Fig. 11a). On the contrary, a lower wave trough exists over the second concave obstacle in Fig. 11(b). Similar to the single obstacle case, a small elevation appears upstream before the fall. The reduction of the amplitude of the second obstacle contributes to a smaller trapped wave amplitude while

the wavelength remains invariant. Furthermore, the additional obstacle's polarization does not affect the wavelength; in both cases, the first obstacle has the same size, and the numerically calculated wavelengths are close, with a relative difference of less than 7%. We, therefore, conclude that the wavelength of trapped waves between two obstacles depends primarily on the obstacle at the origin, which is responsible for the hydraulic fall, and the additional obstacle can be considered as a perturbation to the critical state, which makes the solution jump on a wavy solution temporarily. The same conclusion was drawn for trapped waves upstream in the pure gravity case in Ref. 46.

The wavelength of trapped waves can be inferred from the downstream linear dispersion relation. Figure 12 presents the dispersion relations of the case shown in Fig. 11 when only the first obstacle at the center is considered. The theoretical wavelength of downstream trapped waves can be estimated by solving for the wavenumber in Eq. (9) with the downstream Froude number computed. In Fig. 12, there is no intersection point between the horizontal line of the upstream Froude number and the upstream dispersion relation, which means no trapped waves upstream. The wavelength calculated using the downstream Froude number, denoted by λ_t, is $\lambda_t \approx 5.984$ and is very close to the numerical results. This coherence demonstrates that once the hydraulic fall solution is known, the wavelength of trapped waves caused by an additional obstruction downstream can be predicted by the linear dispersion relations.

The solution branch in the $E_b - F$ plane (with $E_b \leqslant 10$) is shown in Fig. 13(a) for the channel bottom topography characterized by $(A_1, L_1, x_1) = (0.1, 5, 0)$ and $(A_2, L_2, x_2) = (0.05, 5, 20)$. Multiple turning points show that the trapped wave solution is not unique for one bottom configuration. Figure 13(b) gives five different solutions for $F_{1d} = 0.904$ for various values of E_b, namely $E_b = 0.166, 0.423, 0.919, 1.790$ and 4.600. The wavelength of the trapped wave becomes larger with the increase of E_b.

When the second obstacle is placed upstream, there are no trapped waves between the two. The interface features a soliton-like form, in Fig. 14 right above the second obstacle, akin to the phenomenon in the single-layer flexural-gravity and gravity-capillary cases[34,35]. Unlike the pure gravity case with the second obstacle placed downstream in the same regime described in Ref. 46, the soliton-like form is an elevation above a concave obstacle and a depression above a convex obstacle. The structure in the pure gravity case is the opposite; the obstacle and soliton-like wave above are of the same phase. The reason for this difference is that the additional obstruction is found in supercritical flow in the pure gravity case and subcritical flow in the flexural-gravity case, and the local soliton-like solution is opposite based on the analyses in phase planes. With smaller values of E_b, decaying oscillations appear in the tails of the soliton-like wave profiles (see the dotted-line case in Fig. 14b).

Numerical results for Regime (II) are presented in Fig. 15. Similarly, trapped waves downstream between obstacles are considered. The existence of trapped waves downstream can be inferred from Fig. 16, and the theoretical wavelength predicted agrees well with the numerically calculated values.

The solution branch in the $E_b - F$ plane is shown in Fig. 17(a) for the bottom topography characterized by $(A_1, L_1, x_1) = (-0.08, 5, 0)$ and $(A_2, L_2, x_2) = (-0.04, 5, 20)$. The non-uniqueness of solutions is demonstrated in Fig. 17(b), in which different solutions exist for the same downstream Froude number $F_{1d} = 0.302$ and various values of E_b ($E_b = 0.140, 0.333, 0.655, 1.120$). The wavelength of the trapped wave grows with the parameter E_b, which is similar to the tendency in Regime (I). Here, three main families of solutions exist in the branch, categorized by the number of wave crests between two obstacles. Besides being distinct from the branch shown in Fig. 13, which has four primary families, in Regime (II), as E_b increases, the transition between solution families is more natural without any change of bifurcation point. By increasing the parameter E_b, the downstream Froude number decreases overall in Regime (I) while augments in Regime (II).

The soliton-like wave profiles are presented in Fig. 18 for cases where the additional obstacle is placed upstream. Akin to Regime (I), an elevation exists above a concave obstacle, while depression is found above a convex obstacle.

Similar numerical experiments are carried out for Regime (III), namely subcritical flow upstream with critical depth past two successive obstacles of arbitrary polarization. Figures 19 and 20 show typical trapped wave profiles with the second obstacle placed downstream. The theoretical wavelengths are predicted by the linear dispersion relations shown in Figs. 21(a) and 21(b), respectively, close to the computed values. The soliton-like solutions are plotted in Figs. 22 and 23 when the second obstacle is located upstream. The results of cases with a convex obstacle at the center are similar to those in Regime (I). In contrast, with a concave obstacle at the center, the results are akin to those in Regime (II).

We remark that we did not manage to find all the possible solutions for each regime and the cases with supercritical flow upstream. The computations of these solutions may require substantial computational costs and possibly slow convergence. The existence and features of these solutions to be discovered are left for future studies.

IV. CONCLUSIONS

Most previous studies on steady hydraulic falls focus on the free-surface/interfacial gravity hydraulic falls over one or successive obstacles. The effects of hydroelasticity were only considered for one-layer flow past localized bottom topography. We have extended the configuration to a two-layer flow past a single or two successive obstacles with the interface modeled as a thin elastic shell. We first derive the corresponding linear dispersion relation. Then following Ref. 46, fully nonlinear hydraulic fall solutions for three typical regimes, *i.e.*, (I) thick upper layer, (II) thick bottom layer, and (III) critical depth, with subcritical flow upstream for different values of E_b, have been found numerically by a boundary integral equation method.

The increase in obstruction size contributes to the rise in

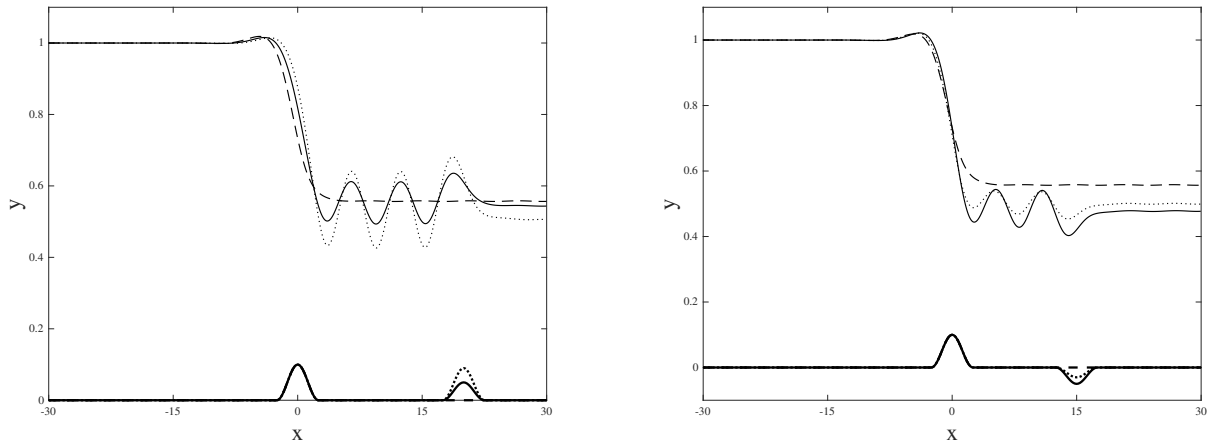

Figure 11. Interfacial hydroelastic hydraulic falls over two obstacles in Regime (I) with $(A_1, L_1, x_1) = (0.1, 5, 0)$ and $E_b = 0.5$. The wave profile for the single obstacle case is presented for comparison (dashed line). (a) Trapped wave solutions between two convex obstacles with $x_2 = 20$ and various aspect ratios of the second obstacle: $(A_2, L_2, \lambda_c) = (0.05, 5, 5.996)$ (solid line); $(A_2, L_2, \lambda_c) = (0.09, 5, 5.884)$ (dotted line). (b) Trapped wave solutions between two obstacles of different phases with $x_2 = 15$ and various aspect ratios of the second obstacle: $(A_2, L_2, \lambda_c) = (-0.05, 5, 5.598)$ (solid line); $(A_2, L_2, \lambda_c) = (-0.03, 5, 5.8)$ (dotted line).

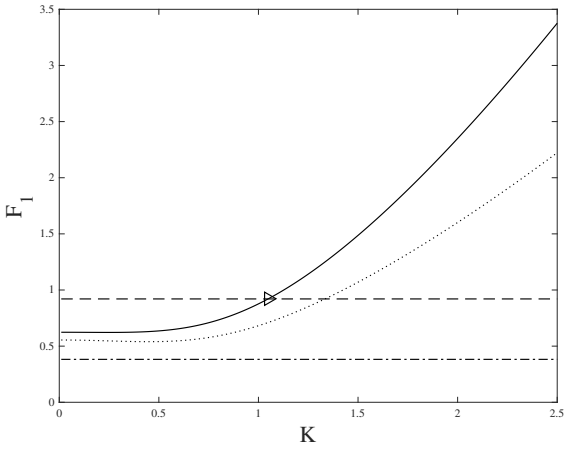

Figure 12. Dispersion relations $F_{1d} = F_{1d}(K)$ (solid line) and $F_{1u} = F_{1u}(K)$ (dotted line) given in Eq. (9) for Regime (I) with $E_b = 0.5$, $A_1 = 0.1$, and $L_1 = 5$ (the dashed line case in Fig. 11). The obtained upstream Froude number (horizontal dash-dotted line) and the obtained downstream Froude number (horizontal dashed line) indicate that trapped wave exists downstream and the theoretical wavelength is $\lambda_t \approx 5.984$ (triangle intersection point).

the difference between the upstream and downstream Froude numbers. A small elevation immediately before the fall in Regime (I) (respective depression in Regime (II)) is observed. With the decrease of the obstruction size and E_b (equivalently the rigidity), the elevation becomes more apparent and part of a train of decaying waves upstream. On the contrary, with a more considerable obstruction, the elevation and the steepness of the fall are weakened. In Regime (III), with the critical depth, the wave profiles depend on the convexity-concavity property of the bottom topography.

When an additional obstruction is placed downstream, a train of trapped waves is found downstream for all three regimes. Variation of the size of the second obstruction exerts little influence on wavelength but has an evident effect on wave amplitude. Numerical computations show that the wavelength of trapped waves can be predicted using the linear dispersion relation and the computed downstream Froude number. The prediction is overall accurate, with only a few percent relative errors. The solution branches in the $E_b - F$ plane indicate the non-uniqueness of solutions for one value of the Froude number. On the other side, waves with a soliton-like form exist above the additional obstruction placed upstream. By decreasing the parameter E_b or the size of the second obstruction, decaying tails start to appear. If E_b has a value small enough so that the upstream Froude number intersects with the linear dispersion relation, trapped waves might exist upstream. However, the computation of corresponding solutions seems challenging to perform.

The numerics for the full Euler equations seem more challenging when the obstacle is concave in Regime (I) (respectively convex in Regime (II)) and the upstream flow is supercritical. We did not manage to find solutions in these regimes for which the computational domain needs to be significant. These cases are also interesting and merit further investigation. Furthermore, in the present work, only the interface is considered an elastic plate, and the top boundary is rigid. Recent studies on computations of solitary waves by including hydroelasticity in both interface and free surface (see Ref. 39) stimulate us to find steady fall solutions in the same configuration in the future.

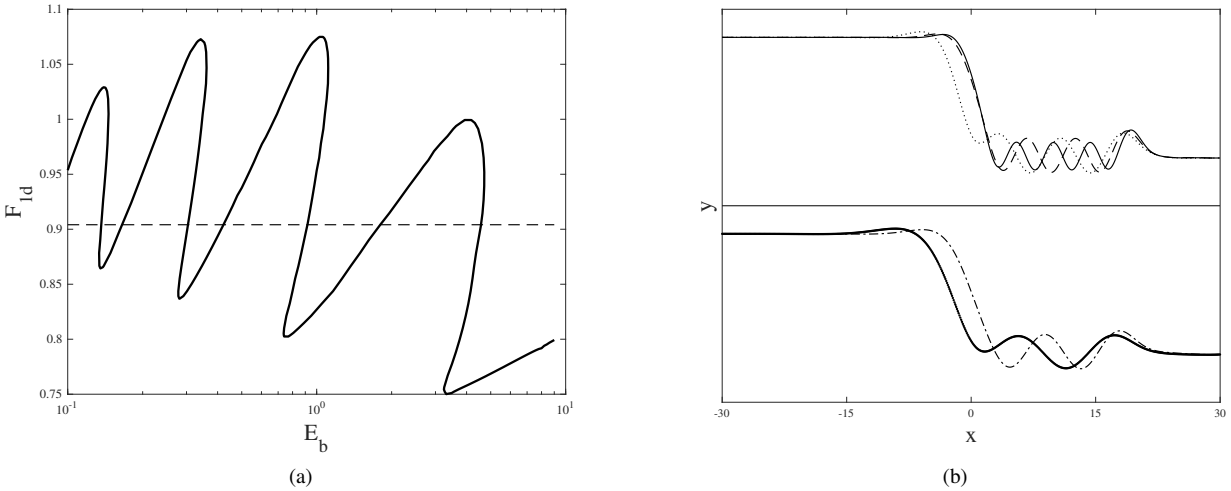

(a) (b)

Figure 13. (a) A solution branch in the downstream $E_b - F_1$ plane for hydraulic falls over two convex obstacles in Regime (I). The obstructions are characterized by: $(A_1, L_1, A_2, L_2) = (0.1, 5, 0.05, 5)$. The horizontal dashed line is $F_{1d} = 0.904$. (b) Trapped wave profiles for the same downstream Froude number ($F_{1d} = 0.904$) and different values of E_b: $E_b = 0.166$ (solid line); $E_b = 0.423$ (dotted line); $E_b = 0.919$ (dashed line); $E_b = 1.790$ (dash-dotted line); $E_b = 4.600$ (bold solid line).

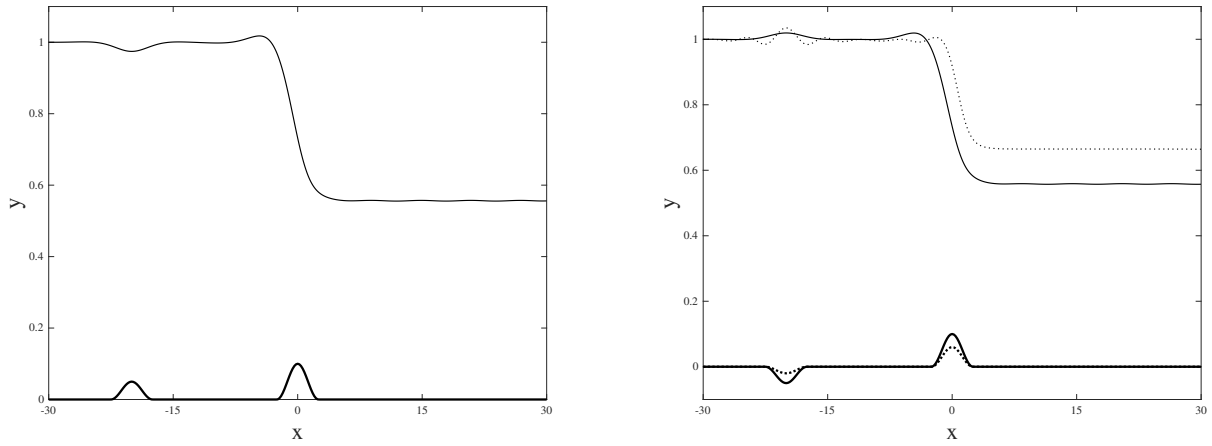

(a) (b)

Figure 14. Interfacial hydroelastic hydraulic falls over two obstacles in Regime (I) with $(A_1, L_1, x_1, E_b) = (0.1, 5, 0, 0.5)$. (a) A soliton-like solution for $(A_2, L_2, x_2) = (0.05, 5, -20)$. (b) A soliton-like solution for $(A_2, L_2, x_2) = (-0.05, 5, -20)$ (solid line) and a soliton-like solution with smaller bottom obstacles (dotted line), namely $(A_1, L_1, x_1, E_b) = (0.05, 5, 0, 0.02)$ and $(A_2, L_2, x_2) = (-0.02, 5, -20)$.

ACKNOWLEDGEMENT

This work was supported by the National Natural Science Foundation of China (Nos. 11911530171), the Key Program of the National Natural Science Foundation of China (No. 12132018), and the Royal Society International Exchanges Travel Grant (No. IEC\NSFC\181279).

DATA AVAILABILITY STATEMENT

The data that support the findings of this study are available from the corresponding author upon reasonable request.

REFERENCES

[1] Akers, B. F., Ambrose, D. M., and Sulon, D. W., "Periodic traveling interfacial hydroelastic waves with or without mass," Zeitschrift für angewandte Mathematik und Physik **68** (2017).

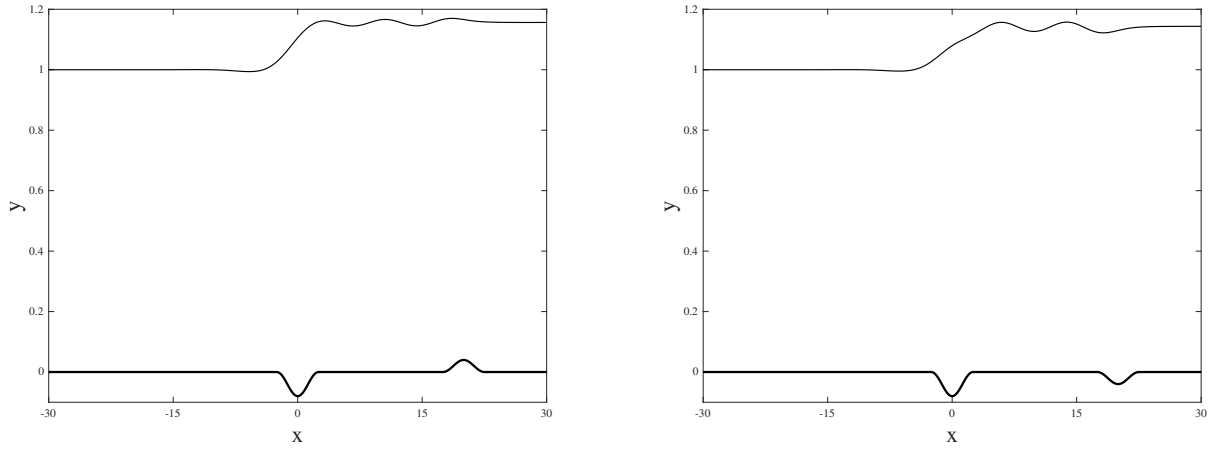

Figure 15. Interfacial hydroelastic hydraulic falls over two obstacles in Regime (II) with $(A_1, L_1, x_1) = (-0.08, 5, 0)$ and $E_b = 0.5$. (a) A trapped wave solution between two obstacles of opposite phases with $x_2 = 20$ and $(A_2, L_2, \lambda_c) = (0.04, 5, 7.702)$. (b) A trapped wave solution between two concave obstacles with $x_2 = 20$ and $(A_2, L_2, \lambda_c) = (-0.04, 5, 7.901)$.

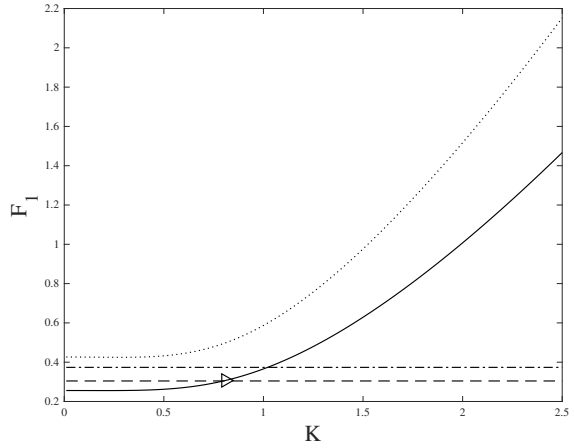

Figure 16. Dispersion relations $F_{1d} = F_{1d}(K)$ (solid line) and $F_{1u} = F_{1u}(K)$ (dotted line) given in Eq. (9) for Regime (II) with $E_b = 0.5$, $A_1 = -0.08$, and $L_1 = 5$ (the case in Fig. 15). The obtained upstream Froude number (horizontal dash-dotted line) and the obtained downstream Froude number (horizontal dashed line) indicate that trapped wave exists downstream and the theoretical wavelength is $\lambda_t \approx 7.757$ (triangle intersection point).

[2] Alben, S. and Shelley, M. J., "Erratum: Flapping states of a flag in an inviscid fluid: Bistability and the transition to chaos [phys. rev. lett. 100, 074301 (2008)]," Phys. Rev. Lett. **101**, 119902 (2008).

[3] Ambrose, D. and Siegel, M., "Well-posedness of two-dimensional hydroelastic waves," Proceedings of the Royal Society of Edinburgh: Section A Mathematics **147**, 529–570 (2017).

[4] Baines, P. G., "A unified description of two-layer flow over topography," Journal of Fluid Mechanics **146**, 127–167 (1984).

[5] Belward, S. and Forbes, L., "Fully non-linear two-layer flow over arbitrary topography," Journal of Engineering Mathematics **27**, 419–432 (1993).

[6] Blyth, M. G., Părău, E. I., and Vanden-Broeck, J.-M., "Hydroelastic waves on fluid sheets," Journal of Fluid Mechanics **689**, 541–551 (2011).

[7] Cabeza, C., Varela, J., Bove, I., Freire, D., Martí, A., Sarasúa, L., Usera, G., Montagne, R., and Araujo, M., "Two-layer stratified flows over pronounced obstacles at low-to-intermediate froude numbers," Physics of Fluids **21**, 044102 (2009).

[8] Cho, I. H. and Kim, M. H., "Interactions of a horizontal flexible membrane with oblique incident waves," Journal of Fluid Mechanics **367**, 139–161 (1998).

[9] Choi, J., Sun, S., and Shen, M., "Steady capillary-gravity waves on the interface of a two-layer fluid over an obstruction-forced modified k-dv equation," Journal of Engineering Mathematics **28**, 193–210 (1994).

[10] Cummins, P., "Numerical simulations of upstream bores and solitons in a two-layer flow past an obstacle," Journal of Physical Oceanography **25**, 1504–1515 (1994).

[11] Cummins, P., Topham, D., and Pite, H., "Simulated and experimental two-layer flows past isolated two-dimensional obstacles," Fluid Dynamics Research **14**, 105–119 (1994).

[12] Deacon, N., Părău, E., Purvis, R., and Whittaker, R., "Nonlinear flexural waves in fluid filled elastic channels," Journal of Fluids and Structures **52**, 16–36 (2015).

[13] Dias, F. and Vanden-Broeck, J.-M., "Steady two-layer flows over an obstacle," Philosophical Transactions of the Royal Society of London. Series A: Mathematical, Physical and Engineering Sciences **360**, 2137–2154 (2002).

[14] Dias, F. and Vanden-Broeck, J.-M., "On internal fronts," Journal of Fluid Mechanics **479**, 145–154 (2003).

[15] Dias, F. and Vanden-Broeck, J.-M., "Trapped waves between submerged obstacles," Journal of Fluid Mechanics **509**, 93–102 (2004).

[16] Dias, F. and Vanden-Broeck, J.-M., "Two-layer hydraulic falls over an obstacle," European Journal of Mechanics - B/Fluids **23**, 879–898 (2004).

[17] Forbes, L., "Two-layer critical flow over a semi-circular obstruction," Journal of Engineering Mathematics volume **23**, 325–342 (1989).

[18] Forbes, L. K., "Surface waves of large amplitude beneath an elastic sheet. part 1. high-order series solution," Journal of Fluid Mechanics **169**, 409–428 (1986).

[19] Forbes, L. K., "Surface waves of large amplitude beneath an elastic sheet. part 2. galerkin solution," Journal of Fluid Mechanics **188**, 491–508 (1988).

[20] Forbes, L. K. and Schwartz, L. W., "Free-surface flow over a semicircular obstruction," Journal of Fluid Mechanics **114**, 299–314 (1982).

[21] Gao, T., Wang, Z., and Vanden-Broeck, J.-M., "New hydroelastic solitary waves in deep water and their dynamics," Journal of Fluid Mechanics **788**, 469–491 (2016).

[22] Grimshaw, R., "A note on the steady two-dimensional flow of a stratified fluid over an obstacle," Journal of Fluid Mechanics **33**, 293–301 (1968).

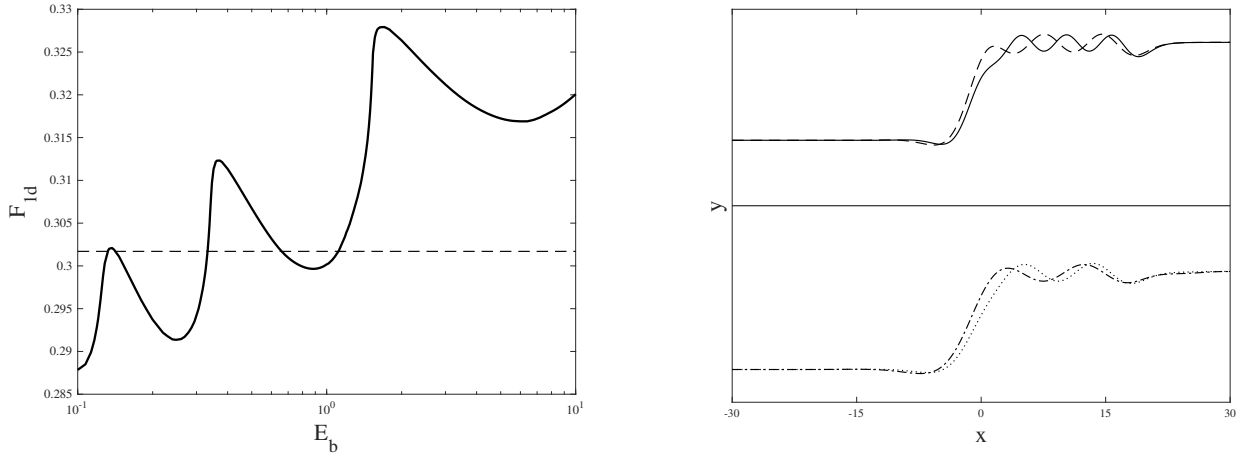

Figure 17. (a) A solution branch in the downstream $E_b - F_1$ plane for hydraulic falls over two concave obstacles in Regime (II). The obstructions are characterized by: $(A_1, L_1, A_2, L_2) = (-0.08, 5, -0.04, 5)$. The horizontal dashed line is $F_{1d} = 0.302$. (b) Trapped wave profiles for the same downstream Froude number ($F_{1d} = 0.302$) and different values of E_b: $E_b = 0.140$ (solid line); $E_b = 0.333$ (dashed line); $E_b = 0.655$ (dotted line); $E_b = 1.120$ (dash-dotted line).

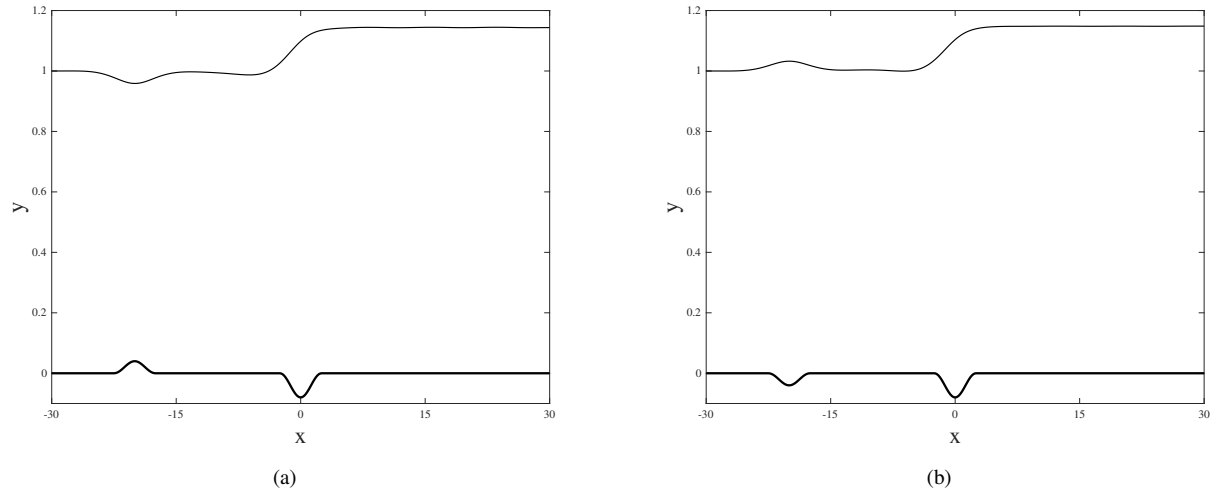

Figure 18. Interfacial hydroelastic hydraulic falls over two obstacles in Regime (II) with $(A_1, L_1, x_1) = (-0.08, 5, 0)$ and $E_b = 0.5$. (a) A soliton-like solution with $(A_2, L_2, x_2) = (0.04, 5, -20)$. (b) A soliton-like solution with $(A_2, L_2, x_2) = (-0.04, 5, -20)$.

[23] Guayjarernpanishk, P.and Asavanant, J., "Free-surface flows over an obstacle: Problem revisited," in *Modeling, Simulation and Optimization of Complex Processes* (Springer Berlin Heidelberg, Berlin, Heidelberg, 2012) pp. 139–151.

[24] Guyenne, P. and Părău, E. I., "Computations of fully nonlinear hydroelastic solitary waves on deep water," Journal of Fluid Mechanics **713**, 307–329 (2012).

[25] Huang, L., "Flutter of cantilevered plates in axial flow," Journal of Fluids and Structures **9**, 127–147 (1995).

[26] Jia, L., Li, F., Yin, X., and Yin, X., "Coupling modes between two flapping filaments," Journal of Fluid Mechanics **581**, 199–220 (2007).

[27] Kim, G. and Davis, D., "Hydrodynamic instabilities in flat-plate-type fuel assemblies," Nuclear Engineering and Design **158**, 1–17 (1995).

[28] Korobkin, A., Părău, E. I., and Vanden-Broeck, J.-M., "The mathematical challenges and modelling of hydroelasticity," Philosophical Transactions of the Royal Society A: Mathematical, Physical and Engineering Sciences **369**, 2803–2812 (2011).

[29] Lawrence, G. A., "The hydraulics of steady two-layer flow over a fixed obstacle," Journal of Fluid Mechanics **254**, 605–633 (1993).

[30] Liu, S. and Ambrose, D. M., "Well-posedness of two-dimensional hydroelastic waves with mass," Journal of Differential Equations **262**, 4656–4699 (2017).

[31] Long, R. R., "Some aspects of the flow of stratified fluids: II. experiments with a two-fluid system," Tellus **6**, 97–115 (1954).

[32] Milewski, P. A., Vanden-Broeck, J.-M., and Wang, Z., "Hydroelastic solitary waves in deep water," Journal of Fluid Mechanics **679**, 628–640 (2011).

[33] Mohapatra, S., Sahoo, T., and Guedes Soares, C., "Surface gravity wave interaction with a submerged horizontal flexible porous plate," Applied Ocean Research **78**, 61–74 (2018).

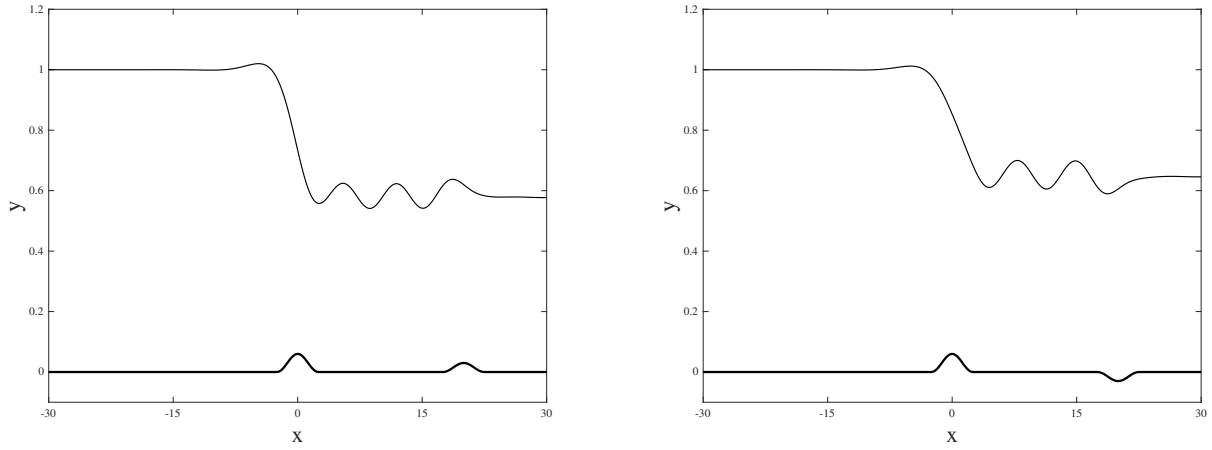

Figure 19. Interfacial hydroelastic hydraulic falls over two obstacles in Regime (III) with $(A_1, L_1, x_1) = (0.06, 5, 0)$ and $E_b = 0.5$. (a) Trapped wave solutions between two convex obstacles with $x_2 = 20$ and $(A_2, L_2, \lambda_c) = (0.03, 5, 6.401)$. (b)Trapped wave solutions between two obstacles of opposite phases with $x_2 = 20$ and $(A_2, L_2, \lambda_c) = (-0.03, 5, 6.993)$.

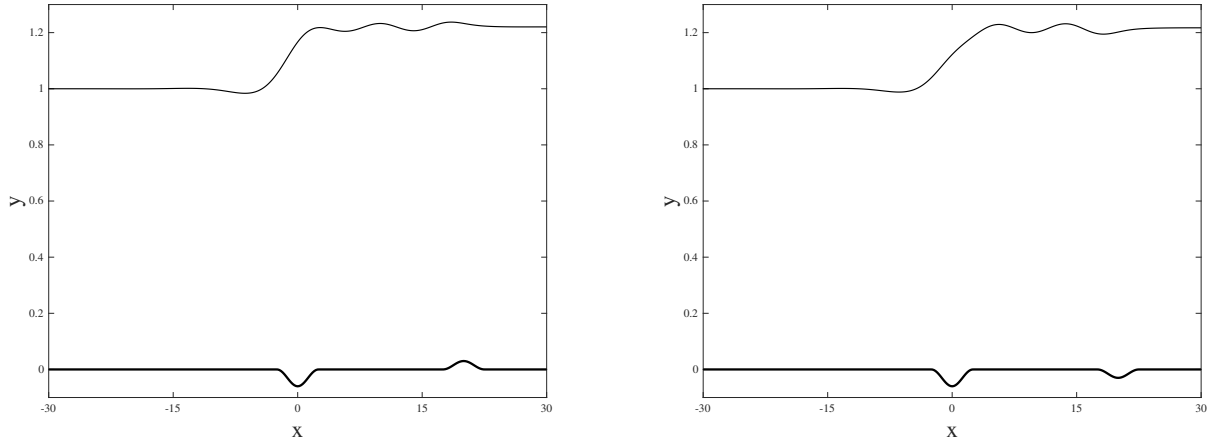

Figure 20. Interfacial hydroelastic hydraulic falls over two obstacles in Regime (III) with $(A_1, L_1, x_1) = (-0.06, 5, 0)$ and $E_b = 0.5$. (a) Trapped wave solutions between two obstacles of opposite phases with $x_2 = 20$ and $(A_2, L_2, \lambda_c) = (0.03, 5, 8.404)$. (b) Trapped wave solutions between two concave obstacles with $x_2 = 20$ and $(A_2, L_2, \lambda_c) = (-0.03, 5, 8.103)$.

[34] Page, C., Grandison, S., and Părău, E., "The influence of surface tension upon trapped waves and hydraulic falls," European Journal of Mechanics - B/Fluids **43**, 191–201 (2014).

[35] Page, C. and Părău, E. I., "Hydraulic falls under a floating ice plate due to submerged obstructions," Journal of Fluid Mechanics **745**, 208–222 (2014).

[36] P.Guyenne, and Părău, E. I., "Finite-depth effects on solitary waves in a floating ice sheet," Journal of Fluids and Structures **49**, 242–262 (2014).

[37] Plotnikov, P. I. and Toland, J. F., "Modelling nonlinear hydroelastic waves," Philosophical Transactions of the Royal Society A: Mathematical, Physical and Engineering Sciences **369**, 2942–2956 (2011).

[38] Părău, E. and Dias, F., "Nonlinear effects in the response of a floating ice plate to a moving load," Journal of Fluid Mechanics **460**, 281–305 (2002).

[39] Părău, E. I., "Solitary interfacial hydroelastic waves," Philosophical Transactions of the Royal Society A: Mathematical, Physical and Engineering Sciences **376**, 20170099 (2017).

[40] Sha, H. and Vanden-Broeck, J.-M., "Two-layer flows past a semicircular obstruction," Physics of Fluids A: Fluid Dynamics **5**, 2661–2668 (1993).

[41] Shen, S.-P., "Forced solitary waves and hydraulic falls in two-layer flows," Journal of Fluid Mechanics **234**, 583–612 (1992).

[42] Squire, V. A., "Past, present and impendent hydroelastic challenges in the polar and subpolar seas," Philosophical Transactions of the Royal Society A: Mathematical, Physical and Engineering Sciences **369**, 2813–2831 (2011).

[43] Squire, V. A., Dugan, J. P., Wadhams, P., Rottier, P. J., and Liu, A. K., "Of ocean waves and sea ice," Annual Review of Fluid Mechanics **27**, 115–168 (1995).

[44] Toland, J., "Steady periodic hydroelastic waves," Archive for Rational Mechanics and Analysis **189**, 325–362 (2008).

[45] Vanden-Broeck, J.-M. and Părău, E. I., "Two-dimensional generalized solitary waves and periodic waves under an ice sheet," Philosophical Trans-

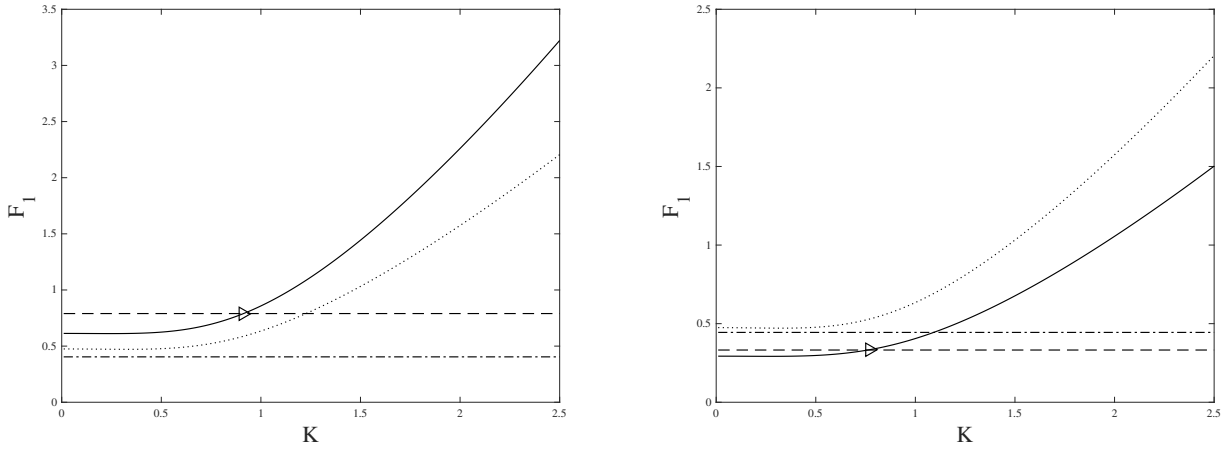

(a) (b)

Figure 21. Dispersion relations $F_{1d} = F_{1d}(K)$ (solid line) and $F_{1u} = F_{1u}(K)$ (dotted line) given in Eq. (9) for Regime (III). The obtained upstream Froude numbers (horizontal dash-dotted lines) indicate that trapped waves only exist downstream. The theoretical wavenumbers can be predicted with the obtained downstream Froude numbers (horizontal dashed lines) for the cases shown in Figs. 19 and 20. (a) $E_b = 0.5$, $A_1 = 0.06$, $L_1 = 5$, and the theoretical wavelength is $\lambda_t \approx 6.756$ (triangle intersection point). (b) $E_b = 0.5$, $A_1 = -0.06$, $L_1 = 5$, and the theoretical wavelength is $\lambda_t \approx 8.160$ (triangle intersection point).

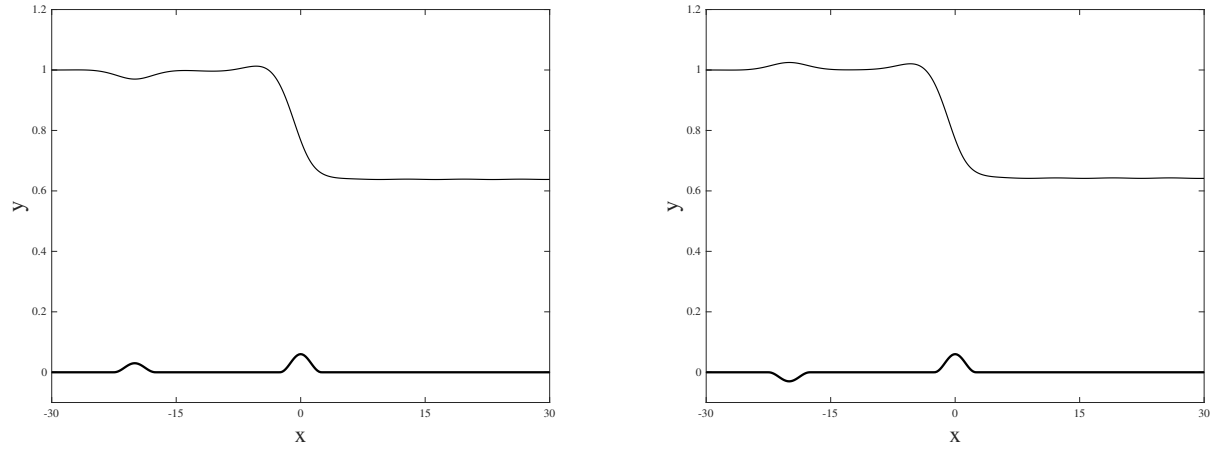

(a) (b)

Figure 22. Interfacial hydroelastic hydraulic falls over two obstacles in Regime (III) with $(A_1, L_1, x_1) = (0.06, 5, 0)$ and $E_b = 0.5$. (a) A soliton-like solution with $(A_2, L_2, x_2) = (0.03, 5, -20)$. (b) A soliton-like solution with $(A_2, L_2, x_2) = (-0.03, 5, -20)$.

actions of the Royal Society A: Mathematical, Physical and Engineering Sciences **369**, 2957–2972 (2011).

[46] Wang, Z., Chai, J., Părău, E. I., Page, C., and Wang, M., "Trapped waves on interfacial hydraulic falls over bottom obstacles," Physical Review Fluids **7**, 074801 (2022).

[47] Wang, Z., Părău, E. I., Milewski, P. A., and Vanden-Broeck, J.-M., "Numerical study of interfacial solitary waves propagating under an elastic sheet," Proceedings of the Royal Society A: Mathematical, Physical and Engineering Sciences **470**, 20140111 (2014).

[48] Wang, Z., Vanden-Broeck, J.-M., and Milewski, P. A., "Two-dimensional flexural–gravity waves of finite amplitude in deep water," IMA Journal of Applied Mathematics **78**, 750–761 (2013).

[49] Xia, X. and Shen, H., "Nonlinear interaction of ice cover with shallow water waves in channels," Journal of Fluid Mechanics **467**, 259–268 (2002).

[50] Xu, Z., Lou, S., Tian, J., and Shen, S.-P., "On hydraulic falls of two-layer flow," Acta Oceanologica Sinica **15**, 179–191 (1996).

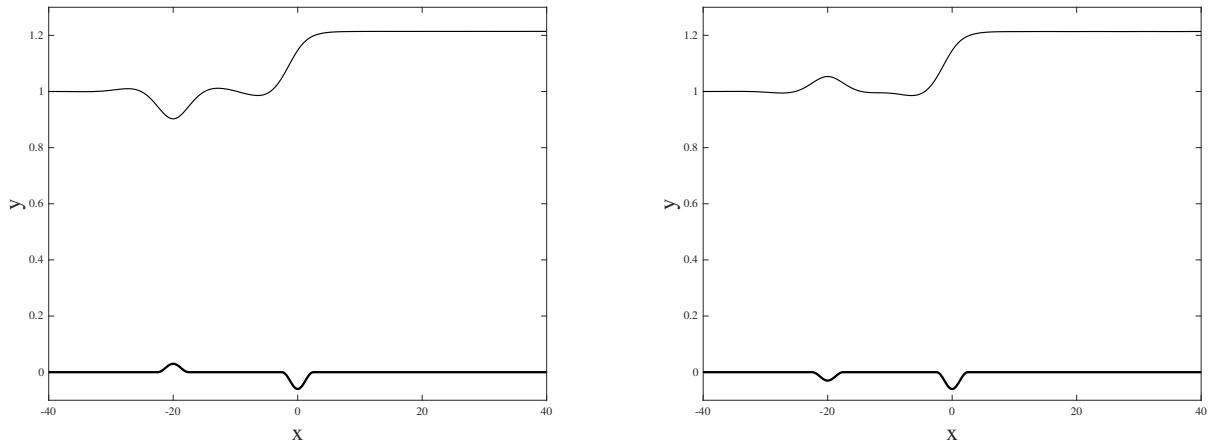

(a) (b)

Figure 23. Interfacial hydroelastic hydraulic falls over two obstacles in Regime (III) with $(A_1, L_1, x_1) = (-0.06, 5, 0)$ and $E_b = 0.5$. (a) A soliton-like solution with $(A_2, L_2, x_2) = (0.03, 5, -20)$. (b) A soliton-like solution with $(A_2, L_2, x_2) = (-0.03, 5, -20)$.